PHYSICAL REVIEW D

PARTICLES AND FIELDS

THIRD SERIES, VOLUME 41, NUMBER 11 1 JUNE 1990

# Determination of electroweak parameters from the elastic scattering of muon neutrinos and antineutrinos on electrons

L. A. Ahrens, S. H. Aronson, P. L. Connolly,[a] B. G. Gibbard, M. J. Murtagh, S. J. Murtagh,[b] S. Terada,[c] and D. H. White[d]
*Physics Department, Brookhaven National Laboratory, Upton, New York 11973*

J. L. Callas,[e] D. Cutts, M. V. Diwan,[f] J. S. Hoftun, B. W. Hughlock,[g] R. E. Lanou, and T. Shinkawa[h]
*Department of Physics, Brown University, Providence, Rhode Island 02912*

Y. Kurihara[h]
*Department of Physics, Hiroshima University, Hiroshima 730, Japan*

K. Amako and S. Kabe
*National Laboratory for High Energy Physics (KEK), Ibaraki-Ken 305, Japan*

Y. Nagashima, Y. Suzuki,[i] S. Tatsumi,[j] and Y. Yamaguchi[k]
*Physics Department, Osaka University, Toyanaka, Osaka 560, Japan*

K. Abe,[h] E. W. Beier, D. C. Doughty,[l] L. S. Durkin,[m] S. M. Heagy,[n] M. Hurley,[o] A. K. Mann, F. M. Newcomer, H. H. Williams, and T. York[p]
*Department of Physics, University of Pennsylvania, Philadelphia, Pennsylvania 19104*

D. Hedin,[q] M. D. Marx, and E. Stern[r]
*Department of Physics, State University of New York, Stony Brook, New York, 11794*
(Received 27 October 1989)

Total and differential cross sections for $\nu_\mu e \to \nu_\mu e$ and $\bar{\nu}_\mu e \to \bar{\nu}_\mu e$ are measured. Values for the model-independent neutral-current couplings of the electron are found to be $g_V = -0.107 \pm 0.035(\text{stat}) \pm 0.028(\text{syst})$ and $g_A = -0.514 \pm 0.023(\text{stat}) \pm 0.028(\text{syst})$. The electroweak mixing parameter $\sin^2\theta_W$ is determined to be $0.195 \pm 0.018(\text{stat}) \pm 0.013(\text{syst})$. Limits are set for the charge radius and magnetic moment of the neutrino as $(\langle r^2 \rangle) < 0.24 \times 10^{-32}$ cm$^2$ and $f_\mu < 0.85 \times 10^{-9}$ Bohr magnetons, respectively.

## I. INTRODUCTION

This paper describes an experiment (E734) to measure $\nu_\mu e \to \nu_\mu e$ and $\bar{\nu}_\mu e \to \bar{\nu}_\mu e$ scattering. It was performed at the Alternating Gradient Synchrotron (AGS) of the Brookhaven National Laboratory with a muon-neutrino beam of mean energy $\approx 1.0$ GeV and a highly segmented, fully active 170-ton detector.[1] The reactions involved are the simplest of the neutral-current reactions; they are purely leptonic with low $Q^2$ and are not complicated by corrections due to strong or electromagnetic interactions nor by thresholds. They occur purely through the weak neutral current; the cross sections have a simple dependence on $\sin^2\theta_W$. The two-body kinematics allow for exact theoretical calculations, and the kinematics also facilitate identification of the signal in the E734 detector. Consequently precise measurements on these reactions provide essential tests of models for electroweak interactions.[2-4]

### A. Kinematics

The two-body scattering reactions

$$\nu_\mu e \to \nu_\mu e \ , \tag{1}$$

$$\bar{\nu}_\mu e \to \bar{\nu}_\mu e \tag{2}$$

can be usefully described by a single kinematic quantity. The quantity of choice in this experiment is the laboratory angle of the recoiling electron with respect to the

 

direction of the neutrino. Conservation of energy and momentum relates the incident neutrino energy $E_\nu$ to the direction and the kinetic energy $T_e$ of the recoiling electron:

$$\cos\theta = \frac{T_e(1+m_e/E_\nu)}{(T_e^2+2T_e m_e)^{1/2}} . \tag{3}$$

Since $m_e \ll T_e$ and $m_e \ll E_\nu$ appropriate approximations lead to a simple limit on the observed angle of the electron:

$$\theta^2 < \frac{2m_e}{T_e} . \tag{4}$$

In this experiment, all the electrons observed from these reactions have angles less than 0.005 rad$^2$ with respect to the nominal neutrino beam direction. Consequently, the signature for neutrino-electron elastic scattering is an event which contains only a single forward electromagnetic shower with the kinematic constraint of expression (4) above.

### B. Phenomenology

The cross sections for reactions (1) and (2) can be written in a model-independent form in terms of the vector and axial-vector couplings ($g_V$ and $g_A$, respectively) between the electron and the neutral, intermediate vector boson ($Z^0$). However, in the standard model of Glashow, Weinberg, and Salam (GWS), $g_V$ and $g_A$ are given by

$$g_V = -\tfrac{1}{2} + 2\sin^2\theta_W , \tag{5}$$

$$g_A = -\tfrac{1}{2} . \tag{6}$$

The relation of the mixing parameter $\sin^2\theta_W$ to the Fermi coupling ($G_F$), the electron charge ($e$), and the mass of the charged, intermediate vector boson ($M_W$) is

$$\frac{G_F}{\sqrt{2}} = \frac{e^2}{8M_W^2\sin^2\theta_W} . \tag{7}$$

The differential cross sections for $\nu_\mu e \to \nu_\mu e$ and $\bar{\nu}_\mu e \to \bar{\nu}_\mu e$ are then

$$\frac{d\sigma}{dy} = \frac{\rho^2 G_F^2 m_e E_\nu}{2\pi}\left[(g_V \pm g_A)^2 + (g_V \mp g_A)^2(1-y)^2 - (g_V^2 - g_A^2)\frac{m_e y}{E_\nu}\right] , \tag{8}$$

where $y = T_e/E_\nu$; the upper sign is for the neutrino channel and the lower sign is for the antineutrino channel. For accelerator energies, $E_\nu \gg m_e$; the last term in the above differential cross sections is therefore negligible. Integration of the differential cross sections yields in this approximation the total cross sections to be

$$\frac{\rho^2 G_F^2 m_e E_\nu}{2\pi}\left[(g_V \pm g_A)^2 + \tfrac{1}{3}(g_V \mp g_A)^2\right] . \tag{9}$$

The parameters to be determined are $\sin^2\theta_W$ and $\rho$. The ratio of the cross sections $R = \sigma(\nu_\mu e)/\sigma(\bar{\nu}_\mu e)$ gives an expression for $\sin^2\theta_W$ independent of $\rho^2$,

$$R = 3\frac{1-4\sin^2\theta_W + \frac{16}{3}\sin^4\theta_W}{1-4\sin^2\theta_W + 16\sin^4\theta_W} , \tag{10}$$

and is less sensitive to errors on the individual cross sections. The expected cross sections and the ratio $R$ are plotted as functions of $\sin^2\theta_W$ in Fig. 1. The factor $\rho$ quantifies the possibility of the neutral current having a different coupling strength than the charged current. In the standard model $\rho$ is expected to be unity.

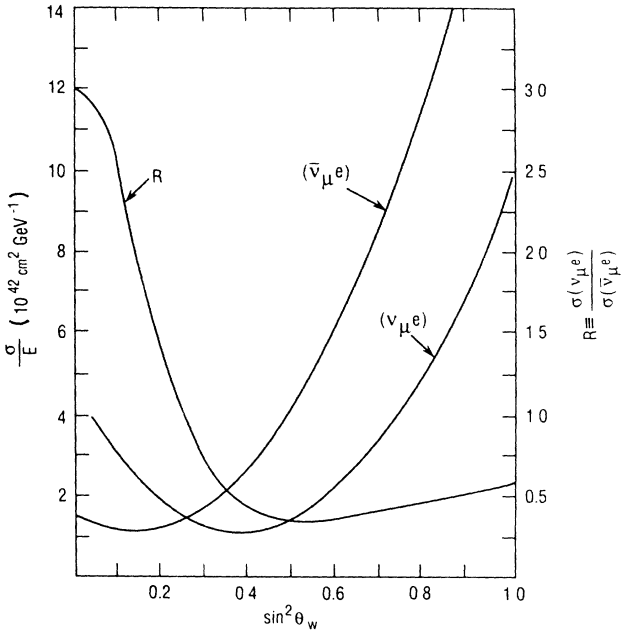


FIG. 1. $\sin^2\theta_W$ dependence of cross sections and the ratio of cross sections.

## II. EXPERIMENTAL PROCEDURE

### A. The neutrino beam

The neutrinos (antineutrinos) in this experiment were the products of decays of pions and kaons which were produced as secondary particles when a proton beam, accelerated to an energy of 28.3 GeV, was bombarded into a sapphire (titanium) target was used for the runs A and B (C). The AGS proton beam was extracted in a single turn and the resulting neutrino beam retained the rf bucket structure of 12 bunches spaced by 224 ns and of ~30 ns width. To obtain a predominantly neutrino (antineutrino) beam, a magnetic horn system was used to focus positive (negative) mesons while defocusing mesons of opposite charge. Further details on the AGS neutrino beam are to be found in Ref. 5.

The muon-neutrino spectra were measured by observing muons, produced by quasielastic interactions in the detector and by determining the muon momentum in the muon magnetic spectrometer located behind the main detector. For low-energy muons, the momentum was

determined from their range in the detector. Since there were also neutrinos of opposite helicity present in the beam, yields of muons of both signs for each horn polarity were measured. The contamination of antineutrinos in the neutrino beam was determined to be $0.043\pm0.007$, and the contamination of neutrinos in the antineutrino beam was determined to be $0.103\pm0.015$. Figure 2 shows the spectra observed.

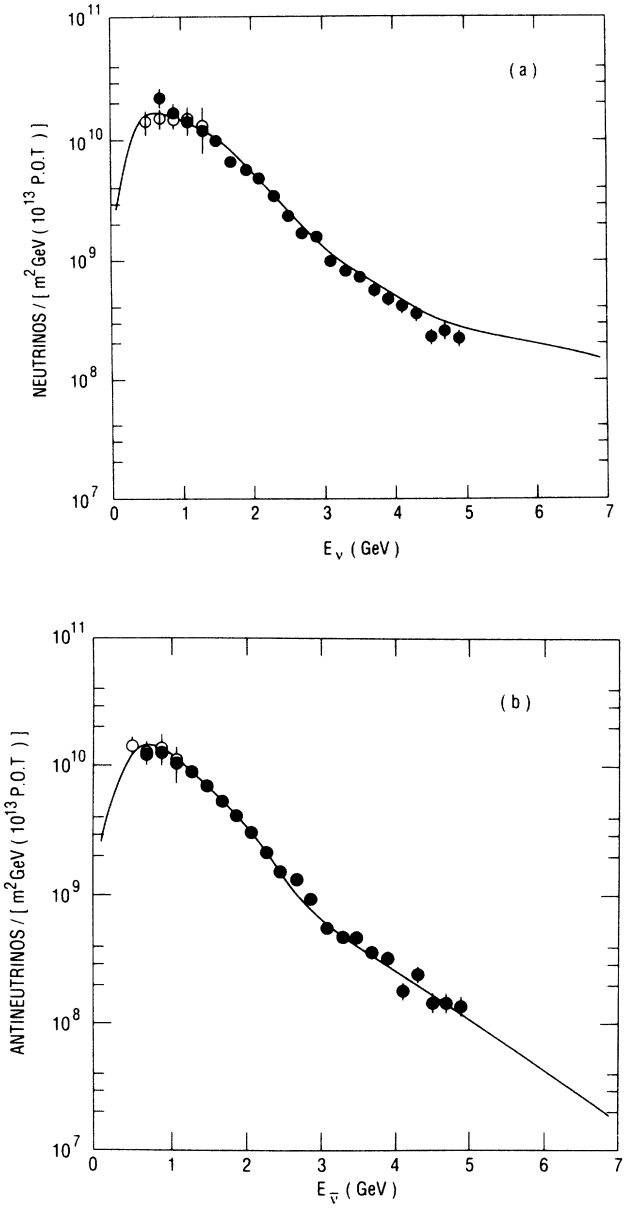


FIG. 2. (a) The $\nu_\mu$ flux. The closed points are data from the magnetic spectrometer; the open points are stopping muon data, and the curve is a calculation done using the computer program NUBEAM for the neutrino beam in run B. The curve has been scaled to correspond to the data. (b) The $\bar{\nu}_\mu$ flux. The closed points are data from the magnetic spectrometer; the open points are stopping muon data, and the curve is a calculation done using the computer program NUBEAM for the antineutrino beam in 1983. The curve has been scaled to correspond to the data.

Electron-neutrinos (antineutrinos) from the sequential decays of kaons and muons were the other source of contamination present in the muon-neutrino (antineutrino) beam. They interacted with nucleons in the detector and produced final-state electrons (positrons) which were a source of background for the neutrino electron elastic-scattering reaction.

Quasielastic reactions $\nu_e n \rightarrow ep$ and $\bar{\nu}_e p \rightarrow en$ were used to obtain the flux of the $\nu_e$ and $\bar{\nu}_e$. The method was similar to the one used in a previous paper by this collaboration (see Ref. 6). The results for this experiment are

$$\frac{\nu_e}{\nu_\mu} = (7.3\pm1.4)\times10^{-3} ,$$

$$2.8\times10^{-3} < \frac{\bar{\nu}_e}{\bar{\nu}_\mu} < 6.1\times10^{-3} .$$

The principal source of uncertainty arises from the calculation of acceptance by Monte Carlo technique. The curves in Fig. 2 are results of beam simulations using the computer program NUBEAM. The above-measured values are consistent with the contamination level calculated using NUBEAM which was approximately $7\times10^{-3}$ for each beam polarity. For a complete description and additional references see Ref. 6.

### B. The E734 detector and its performance

The detector has been extensively described elsewhere[1,7–12] and will be briefly reviewed here. The neutrino beam intensities [approximately $10^{10}$ $\nu_\mu/m^2$ GeV ($10^{13}$ protons on target)], in conjunction with the small cross section for neutrino electron scattering ($10^{-42}$ cm$^2$), demand a large mass detector to obtain useful event rates. The AGS delivered approximately $10^{13}$ protons per pulse. The detector must also provide many measurements of $dE/dx$ along a track for particle identification and excellent angular resolution for forward tracks. These considerations led to the size and the modular design of the E734 detector.

The detector had two major systems: The liquid-scintillator calorimeter viewed by photomultiplier tubes (PMT's) and the proportional-drift-tube (PDT) system. The liquid scintillator, NE235A mixed with mineral oil, served as a target for neutrinos and also as a detector with fine energy and time resolution. The proportional drift tubes (7.6 cm high, 3.8 cm along the beam, and 4 m long) were used for particle tracking and $dE/dx$ measurements along the track. The main detector was divided in 112 modules. Each module contained a wall of 16 liquid-scintillator cells (25 cm high, 8 cm along the beam, and 4 m long) and an $x$-$y$ plane of 54 proportional drift tubes. Each module was 4 m$\times$4 m in active area, 0.22 radiation lengths in thickness, and had a mass of about 1.5 tons. As an electron traveled through the detector it crossed about 5 modules within one radiation length permitting multiple measurements of position and energy deposits along the track before significant multiple scattering and radiation had occurred.

The total mass of the detector was 170 tons. The mass of the fiducial region used for reactions (1) and (2) was about 70 tons. About 90% of the mass was in liquid scintillator. After the main detector there was a shower detector, which consisted of ten walls of liquid-scintillator cells with a one-radiation-length sheet of lead after each wall. There were no PDT's in the shower detector. Ten radiation lengths were considered sufficient to measure electromagnetic showers originated at the end of the main detector.

The detector was at the end of the neutrino beam line at the Brookhaven AGS, 147.8 m downstream from the target. The neutrino beam was fully contained by the detector with beam center offset by approximately 30 cm from the detector center line. The main part of the detector was 21 m long and 4.2×4.2 m in cross section.

At the very end of the detector there was an air gap, magnetic spectrometer[5] to measure the momentum of muons produced in the main detector. It had an aperture of 1.8×1.8×0.46 m. The magnetic field imparted transverse momentum of 40 MeV/$c$ at the center and 70 MeV/$c$ at the edge. Nine pairs of PDT planes, four before the magnet and five after, served to measure the bend of a particle track, which was fit to a parabola. The start time for the drift measurements was generated from the last six calorimeter walls in the main detector. Uncertainties in the PDT positions, about 1.3 mm, limited the momentum resolution to

$$\frac{\delta p}{p}=\sqrt{0.010+[0.067p/(\mathrm{GeV}/c)]^2}\ .$$

A typical data accumulation cycle began when a pulse of protons, 2.7 $\mu$s wide and with the bunch structure described earlier, hit the target. The repetition rate of bursts of 28.3-GeV protons from the AGS was 1.4 s. On average 1.5 $\nu_\mu$-induced events were obtained in the detector per pulse. A 10-$\mu$s gate, opened at the same time as the proton beam extraction, enabled all detector elements to record data. The electronics associated with each detector element, a PMT or a PDT, was able to record the total energy deposition in that element and at least two pulse times with little dead time. After the end of the 10-$\mu$s gate the data were read out and recorded on magnetic tape by computers. The entire process, taking no more than 50 ms, provided ample time to perform monitoring and calibration procedures between beam bursts.

A portion of the E734 detector was placed in a test beam at BNL (Refs. 10–12). Using this test setup data were taken for several tagged particle types and momentum ranges. The information was used to establish ionization profiles for different particles. Many of the analysis procedures were tested on these data.

Of particular value to this experiment were data from test beam electrons with energies of 0.4, 0.6, 0.8, and 1.0 GeV which were taken in the test detector. The known incident angle, determined from beam wire chambers, was compared with the angle measured in an interactive process fitting each projection of the detector and thus an angular resolution function was obtained

$$\Delta\theta_{x,y}=\frac{13\pm1\ \mathrm{mrad}}{\sqrt{E_e\ (\mathrm{GeV})}}\ .$$

The known energy of the electron was compared with the energy measured in the test detector to obtain both the energy resolution function and a scale factor to account for the energy lost in the inactive parts of the detector. The energy resolution function obtained as

$$\frac{\Delta E}{E}=\frac{0.13}{\sqrt{E\ (\mathrm{GeV})}}\ .$$

The scale factor in the main detector was 1.43±0.14. In the shower counter the scale factor was estimated to be 2.5±0.2. The scale factor was also studied using Monte Carlo simulations and kinematically reconstructing $\nu_e n\rightarrow e^- p$ events seen in the main detector. Both the scale factors were found to be consistent within 10%. Figure 3 shows the energy and angular resolution for electron-induced showers in the detector.

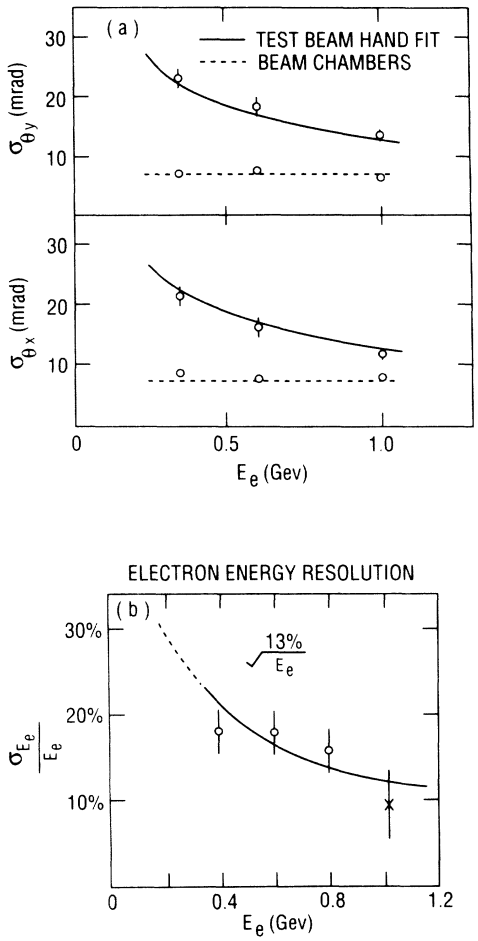


FIG. 3. (a) Angular resolution of electrons in the test beam detector from a hand fit to the PDT data. (b) Energy resolution of electrons in the test beam detector.

## III. DATA REDUCTION

The E734 detector accumulated data in three different runs (hereafter referred to as runs A, B, C, respectively) from exposure to the wideband neutrino or antineutrino beam since first becoming operational in 1981. A portion of these data were analyzed for neutrino and antineutrino electron scattering, and were the subject of previous papers.[13–16] As additional data accumulated, the analysis routines were refined. This paper presents the entire sample of $\nu_\mu e \to \nu_\mu e$ and $\bar{\nu}_\mu e \to \bar{\nu}_\mu e$ elastic-scattering events from E734.

Since the distances inside the decay tunnel and the target were changed subsequent to run B, the spectra of neutrinos and antineutrinos from runs A and B were compared to the spectra obtained in run C, the third long running period.[5,17] All components of the run C spectrum had the same energy distribution as the runs A and B spectra. The total intensities were, however, different. The mean energy of the run-C $\nu_\mu$ ($\bar{\nu}_\mu$) beam was 1.27 (1.28) GeV, which was compared to the value in runs A and B: 1.27 GeV for $\nu_\mu$ (1.19 GeV for $\bar{\nu}_\mu$). 35.1% (40.6%) of the neutrino (antineutrino) data were obtained in run C.

The analysis procedure used for the run C data to obtain a sample of electromagnetic showers was identical to the procedure used for the runs A and B data[11,12] except for some additions to the electron shower recognition procedure. The additions reduced the number of events visually scanned, but they introduced an additional small inefficiency which was properly combined with other corrections to the total number of observed signal events. The normalization procedure was identical for all data sets.

Convinced that the spectra and the analysis methods were almost identical for all the data accumulated and that the errors were well understood, all the final samples of electromagnetic showers were combined and likelihood fits were made to the resulting distributions. Table I shows the combined number of events for the neutrino and antineutrino samples and the final cuts.

### A. The production program

The production program read events from raw data tapes, used calibration and geometry constants for each element to convert raw time and charge information into absolute time and energy depositions, recognized tracks and showers, and produced two sets of data: a set containing single-electron-shower candidates and a set containing muon-neutrino quasielastic candidates for normalization.

The bunch structure of the neutrino beam was reflected in the time distribution of the observed neutrino interactions. The calorimeter hits in each burst were grouped in time clusters to separate overlapping interactions in the pattern of hits. For each event a histogram was made of calorimeter hit times in 40-ns bins. Hits from nonzero bins within two bins of each other were considered to belong to the same time cluster. PDT elements were associated with a time cluster if the PDT time was within a 1-$\mu$s window around the mean time of the cluster. A PDT could be associated with at most three different time clusters.

After time clustering, events were processed through two different algorithms. All events went through the first algorithm, the shower filter which identified events containing potential single electromagnetic showers. Every third event went through the second track fitting algorithm, which fully reconstructed the event and wrote the results in a standardized form onto a dark-summary tape (DST). The quasielastic events, used for normalization, were obtained from these DST's. Events with tracks in the spectrometer were also recorded and later used to calculate the neutrino spectrum.

An electromagnetic shower leaves a characteristic pattern of energy deposition as it traverses the detector. In the initial stages of an energetic shower the secondary particles tend to be produced at very small angles with respect to the original particle. The finite size of the PDT's does not permit us to follow the development of each particle in the shower. However, the secondaries do cause the number of elements hit per plane to increase along the path of the shower. The shower filter algorithm recognized electromagnetic showers of energy above 200 MeV. The algorithm used energy and time clustering information for each event. It also used spatial information from the PDT's to recognize patterns associated with electromagnetic showers. For complete details see Ref. 17.

A small fraction of the data were not processed. During normalization processing some runs were judged to be bad because of calibration or hardware errors. Events belonging to these bad runs were removed from the samples; the normalization was adjusted accordingly.

TABLE I. Data-flow sequence. Numbers refer to the number of events surviving after each step.

| | $\nu_\mu$ | $\bar{\nu}_\mu$ |
|---|---|---|
| POT | $3.42\times10^{19}$ | $4.74\times10^{19}$ |
| Software | 338 686 | 150 437 |
| Visual scan | 12 210 | 4 928 |
| Initial cuts | 2 134 | 1 362 |
| $e/\gamma$ cut | 1 322 | 802 |
| $\theta^2<0.03$ Rad$^2$ | 898 | 572 |

### B. Electron identification

Because of the difficulty and complexity of pattern recognition for electromagnetic showers with software and the need for high signal acceptance, a visual scan by physicists of computer-generated pictures was used to further reduce the sample. Monte Carlo–simulated events overlaid with real beam bursts were randomly inserted among the data at a level of 2% as a control on event recognition efficiency; 93% of the events were scanned twice to assure high efficiency. The electromagnetic portion of the Monte Carlo program was EGS4 (Ref.

18) and its ability to simulate events in this detector was checked extensively against test beam data. The objective of this visual scan was to reject events which were selected by the initial shower filter but which were obviously not single, forward showers. The most obvious examples were forward muons passing through cracks in the detector and multitrack events where the hadron tracks were obvious to the eye but did not have enough deposited energy to fail the single, forward shower criteria.

The resulting shower data sets were processed through a program which calculated various quantities concerning the shower to facilitate analysis. The program evaluated the shower angle using a least-squares fit to the drift distances in the PDT's (calculated from the drift times). The fit encompassed all possible combinations of PDT hits with weighted uncertainties based on the effects of multiple scattering. The total energy of the shower and the energy deposits in the cells of the first six planes were also determined by the program.

Events failing the following criteria were eliminated from the sample.

(1) *Fiducial-volume cut*:

$$7 < X_{\mathrm{PDT}} < 51,\ 7 < Y_{\mathrm{PDT}} < 51,\ 7 < Z_{\mathrm{module}} < 97 .$$

$X_{\mathrm{PDT}}$ and $Y_{\mathrm{PDT}}$ are the cell numbers of the vertex PDT cell, and $Z_{\mathrm{module}}$ is the module number of the vertex. This cut eliminated front and side entering tracks and showers which were not fully contained in the detector (Fig. 4).

(2) *Energy cut*:

$$210 < E_e < 2100 \text{ MeV} .$$

$E_e$ is the total corrected energy of the shower. This cut[11] was effective in reducing low- and high-energy backgrounds. At low energies, $\pi^0$ decays and hadrons dominated whereas quasielastic electron-neutrino interactions dominated above 1500 MeV (Fig. 5).

(3) *Vertex energy cut*:

$$E_{\mathrm{vertex}} < 30 \text{ MeV} .$$

The background events due to hadrons or quasielastic electron-neutrino interactions usually had final-state hadrons with large energy deposits in the vertex cell. Monte Carlo studies suggested that a vertex cell energy of 30 MeV was a reasonable upper limit for the true electron signal (Fig. 6).

(4) *Topology and road cut*: Full exploitation of the high angular resolution of the PDT's was obtained by manual fitting. Each event was displayed on a graphics screen along with the fits obtained by the pattern-recognition programs; using the displayed PDT's and drift distances, the operator iterated fits to the front part of the shower in both views of the event until a satisfactory fit was obtained. The fits obtained by the pattern-recognition programs were chosen if they were judged acceptable. More specifically, the fitting program used the first six PDT's. Using all combinations of left-right ambiguity and weighting uncertainties based upon the effects of multiple

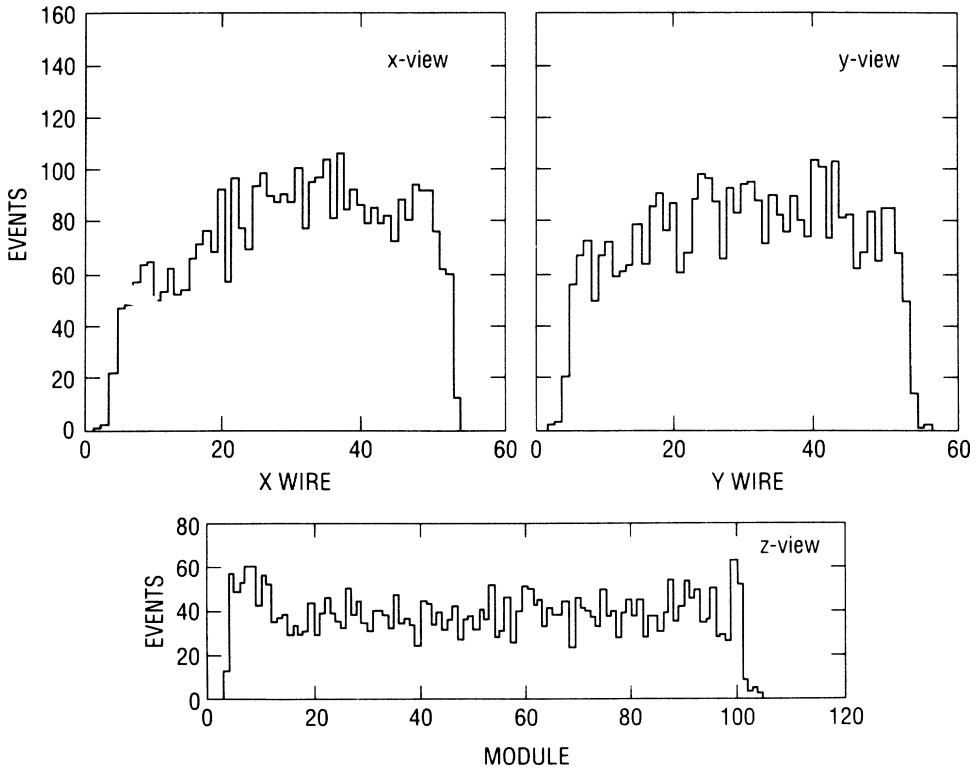


FIG. 4. Vertex position distributions for the neutrino events.

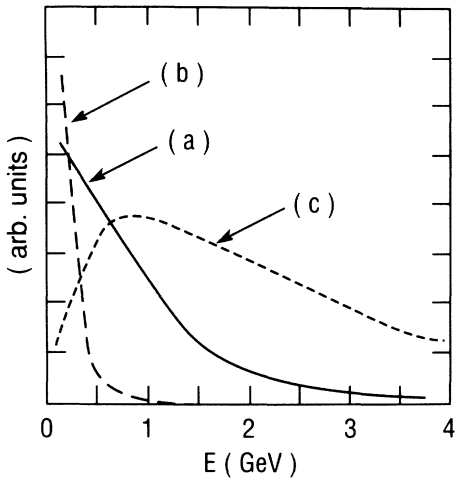


FIG. 5. Monte Carlo simulations of shower energy for (a) $\nu_\mu e \rightarrow \nu_\mu e$, (b) photons from the pion in $\nu_\mu + n \rightarrow \nu_\mu + n + \pi^0$, and (c) $\nu_e n \rightarrow e^- p$. Distributions for the antineutrino reactions are similar.

scattering it calculated the angle of the track. The program failed an event when the $\chi^2$ minimization produced the wrong combination of left-right drift times because of wrong measurement of time in one of the PDT's, overlapping hits or inefficiencies in one of the most forward PDT's. In manual fitting we looked at the fits to see if any of the above were causing an incorrect fit. No systematic bias was found to result from the manual fits.

The showers from hadronic interactions and showers from overlapping photons of $\pi^0$ decays tend to be broad. Multiple scattering makes them deposit much more energy away from the center of the shower than electron showers of similar energy. A "maximum multiple scattering road" was applied to the showers; the road was based on the maximum scattering limits of a single electron computed by using the standard electromagnetic-shower simulation, EGS (Ref. 18). A line, 20 modules long, was also drawn upstream of the shower vertex. The program displayed the sum of the shower energy outside the road and the sum of the energy directly upstream within 20 modules of the vertex. The operator rejected the event (1) if the energy outside the road was greater than 2.5% or (2) if there was greater than 10 MeV deposited directly upstream. The operator exempted events from the above criteria if it was judged that the energy determinations were complicated by unassociated interactions in the same time bucket.

(5) $e/\gamma$ *cut*: The event samples, after the above selections, were predominantly either electrons (e) or photons ($\gamma$). The PDT and scintillator $dE/dx$ measurements near the vertex were used to eliminate as many of the photons as possible. Monte Carlo and test beam studies of single electrons and $e^+e^-$ pairs suggested that true electrons appeared initially with high probability ($>90\%$) as singly ionizing tracks and true photons appeared ($>70\%$) as doubly ionizing tracks. A sample of showers expected to be due to photons because they pointed towards other energy deposits (stubs) upstream in the detector, was analyzed similarly. The $dE/dx$ distributions for the stub sample clearly shows that it was composed of doubly ionizing particles, as expected for photons. Figure 7 illustrates the $dE/dx$ distributions for test beam electrons and stub data.

The $dE/dx$ algorithm was based upon the energy deposited in the first scintillator cell after the vertex cell and a combination of adjacent PDT cells. The PDT's being low-mass devices have a large probability for registering no energy; their $dE/dx$ distributions also have long Landau tails, and so a truncated mean approach was used to determine PDT $dE/dx$. Both $x$ and $y$ PDT's on the track in the two planes after the vertex were used. If a PDT had no energy it was excluded from further calculation. The minimum of the two energies in each plane was determined, and their mean was used as the measure of PDT $dE/dx$. The following region was designated as the photon region:

$$dE/dx(\text{cal}) \equiv E_{\text{cal2}} > 18 \text{ MeV}$$

and

$$dE/dx(\text{PDT}) = \frac{\min(E_{x_1}, E_{y_1}) + \min(E_{x_2}, E_{y_2})}{2}$$

$$\equiv E_{\text{av23}} > 15 \text{ keV} .$$

Any event not classified as a photon was considered an electron. See Fig. 8 for $dE/dx$ distributions of the neu-

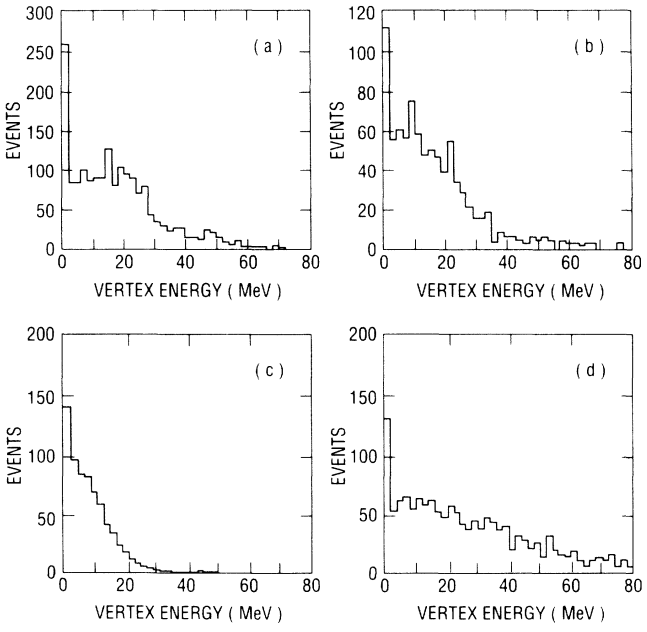


FIG. 6. Vertex energy for (a) the neutrino sample, (b) the antineutrino sample, (c) $\nu_\mu e \rightarrow \nu_\mu e$ Monte Carlo sample, (d) $\nu_e + n \rightarrow e^- + p$ Monte Carlo sample. (Events that have no calorimeter hit in same plane as the first PDT are assigned zero vertex energy.)

trino data.

(6) $\theta^2 < 0.03$ *rad*$^2$ *cut*: Since there were hardly any ($<1\%$) signal events beyond 0.03 rad$^2$, all events with $\theta^2 > 0.03$ rad$^2$ were discarded.

The selected electron and photon candidates are shown in Fig. 9. There are no sharp peaks in the photon angular distributions. The forward peaks in the electron distributions are due to the neutrino (antineutrino) electron elastic scattering signal events.

### C. Signal extraction

After all the analysis cuts, each shower event was characterized by four quantities: $\theta^2$, square of the measured angle; $T_e$, total energy of the shower; $E_{\text{cal2}}$, measure of $dE/dx$ in calorimeters, and $E_{\text{av23}}$, measure of $dE/dx$ in PDT's. Since the $\theta^2$ and $T_e$ distributions, obtained after the $e/\gamma$ cut, showed the most obvious manifestations of the signal events, likelihood fits were made incorporating both variables to extract the total number of signal events in both the neutrino and antineutrino data. To extract the number of signal events under the peak in the $\theta^2$ distribution, it was necessary to understand and find a true representation of the background.

### D. Backgrounds

Monte Carlo events were generated and the background distributions were studied taking into account all smearing effects in the detector and measurements. A full description of event simulation algorithms for this experiment is contained in Ref. 10. The $\theta^2$ distribution was divided in two parts for background studies. The region above 0.01 rad$^2$ was considered the background region because it contained less than 7% of the signal. The energy and $dE/dx$ distributions of the background region were consistent with the assumption that it consisted mostly of photons from pion decays and electrons or positrons from the electron-neutrino quasielastics ($\nu_e n \rightarrow ep$

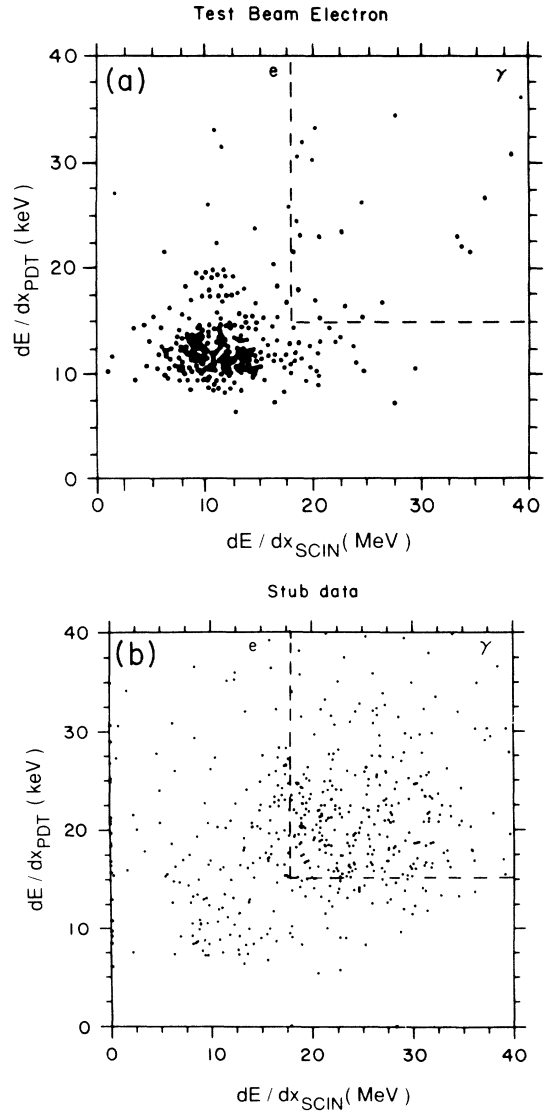


FIG. 7. $dE/dx$ distributions for (a) test beam electrons and (b) showers pointing to upstream deposits ("photons," see text).

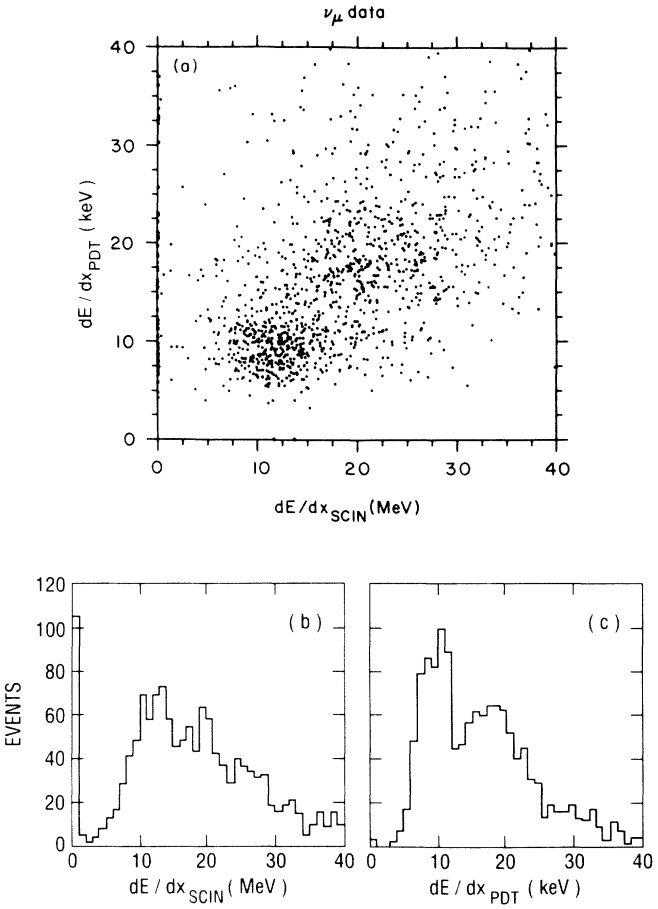


FIG. 8. $dE/dx$ distributions for all neutrino data. (a) Scatterplot of $E_{\text{cal2}}$, measure of $dE/dx$ in calorimeters and $E_{\text{av23}}$, measure of $dE/dx$ in PDT's. (b) Projection for $E_{\text{cal2}}$. (c) Projection for $E_{\text{av23}}$.

for the neutrino data and $\bar{\nu}_e p \rightarrow en$ for the antineutrino data). Possible presence of low-energy hadrons was studied[11,12] visually and by examining events having the mean number of PDT hits per plane less than 1.3, since low-energy hadrons were not expected to shower. The observed $\theta^2$ distribution of these events did not differ significantly from the distribution due to $\pi^0$ decays. The fraction of low-energy hadronic events in the background was negligible for the final sample.

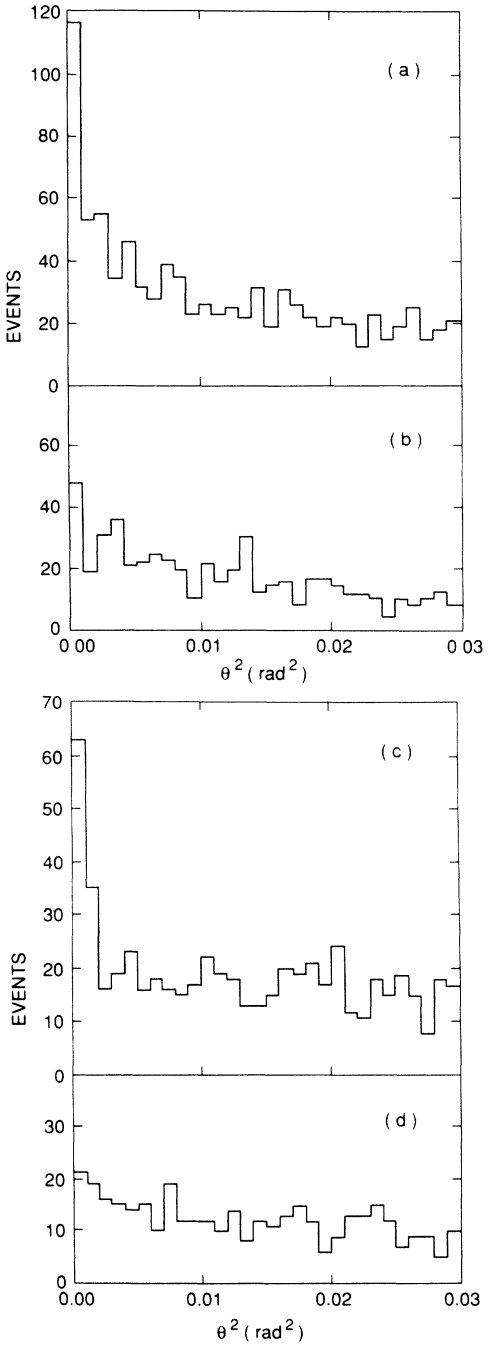


FIG. 9. $\theta^2$ distributions for all neutrino data: (a) Electrons identified by the $e/\gamma$ cut. (b) Photons identified by the $e/\gamma$ cut. $\theta^2$ distributions for all antineutrino data: (c) Electrons identified by the $e/\gamma$ cut. (d) Photons identified by the $e/\gamma$ cut.

(1) *The $\pi^0 \rightarrow \gamma\gamma$ background*: The $\pi^0$'s produced in coherent ($\nu N \rightarrow \nu N \pi^0$) and incoherent ($\nu n \rightarrow \nu n \pi^0$ and $\nu p \rightarrow \nu p \pi^0$) neutral-current interactions were the principal candidates for this background.[19] Monte Carlo studies indicated that at AGS energies and with the composition of the E734 detector the coherent production contributed only $0.16 \pm 0.06$ of the total $\pi^0$ background. The error is estimated by propagating the typical measurement errors for cross sections used in the model of Ref. 19. Also the energy and $\theta^2$ distributions of photons from all three channels were so similar for the region of interest that the $\nu n \rightarrow \nu n \pi^0$ channel was considered an adequate representation for the total $\pi^0$ background. The photons produced from the $\pi^0$ decays were uniformly distributed in $\theta^2$ below 0.03 rad$^2$ and were less than 1000 MeV in energy, but at the largest angles the angular resolution of the shower filter in conjunction with angle cuts caused decreased acceptance for events, resulting in a weakly sloped $\theta^2$ distribution beyond the signal region [Figs. 9(b) and 9(d)].

(2) *Background due to electron-neutrino quasielastics ($\nu_e n \rightarrow e^- p$ and $\bar{\nu}_e p \rightarrow e^+ n$)*: The $\theta^2$ distribution for the electron/positron from these events is suppressed in the forward ($<0.01$ rad$^2$), low-$Q^2$ region because of Pauli suppression in the nucleus.[10,20] For $\theta^2 > 0.01$ rad$^2$ the distribution showed the same slope behavior—due to the shower filter—as the $\pi^0$ background. The shape of the $\theta^2$ distribution was affected mainly by the $\theta^2$ acceptance. For the neutrino channel, since the proton left visible energy at the vertex, the vertex cut of 30 MeV was responsible for the nonuniform acceptance in $Q^2$. This was investigated by making cuts on the energy of the final-state nucleon in the Monte Carlo events. For the antineutrino channel, lack of sufficient modeling for the neutron interactions in the detector made such investigation impossible; assumption of uniform acceptance, finally used, was only approximately correct because during visual scanning some events were rejected, the neutron having become visible by an energetic interaction in the detector (Fig. 10). The $\theta^2$ distribution was also weakly dependent on the axial-vector mass $M_A$ and the nuclear scattering

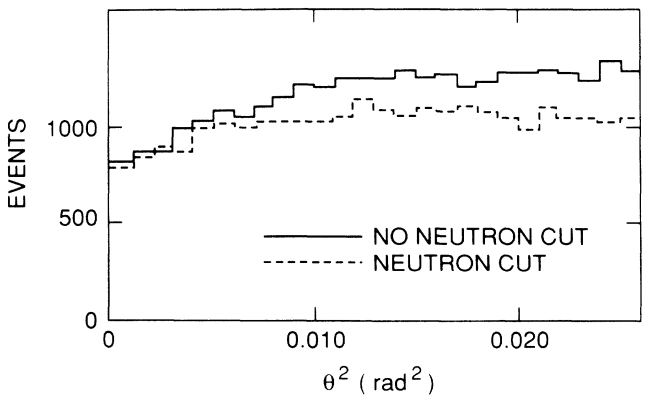


FIG. 10. Study of the $\theta^2$ distribution of $\bar{\nu}_e p \rightarrow en$ by making cuts on the energy of the neutron.

model.[10] Allowances for these uncertainties were made in the systematic errors (Table II).

The $\theta^2$ distribution of the two backgrounds thus established, it was judged most desirable to use for its energy characterization the measured energy distribution of the *data* above 0.01 rad$^2$, i.e., the background region.

The complete background distributions were combinations of the distributions from the two backgrounds (Fig. 11). Because of their slightly different shapes it was necessary to determine the fraction contributed by each of the background channels. The electron-neutrino beam fluxes, measured by using higher-energy electromagnetic-shower events, were used to calculate the fraction of the background due to the quasielastics. The acceptance for these events was computed making use of a full Monte Carlo simulation including detector simulation of these events in the detector and selection of the events by all the electron analysis cuts. The calculation was done by integrating the flux folded with the cross sections and multiplying by the total acceptance. The fraction of $e^-p$ ($e^+n$) expected in the neutrino (antineutrino) data, $f_{ep}$ ($f_{en}$), was 0.23±0.12 (0.41±0.15). The errors on these numbers were large due to uncertainties in acceptance. Therefore, when the final fits to the electron data were made, the *ep/en* fraction was varied within its experimental errors to obtain the best fit to the $E$-$\theta^2$ distribution. The systematic errors due to background simulation are also indicated in Table II.

The final numbers of elastic scattering signal events were obtained by a maximum-likelihood fit in two variables, $\theta^2$ and energy. Signal and background distributions were fit to the data using a log-likelihood function. The signal event distributions were generated from the full Monte Carlo simulation which took account of resolution, acceptance, inefficiency effects and effects due to noise from unrelated events in the same time cluster. The energy distribution for both channels in the background was modeled from the energy distribution of the data for $\theta^2 > 0.1$ rad$^2$, the background region where the number of signal events was expected to be small. The likelihood function for the two-dimensional distribution was obtained by assuming a Poisson probability distribution for each bin. The log-likelihood function is expected as

$$\ln\Phi = \sum_{ij} -\bar{n}_{ij} + n_{ij}\ln(\bar{n}_{ij}) - \ln(n_{ij}!) \ , \tag{11}$$

TABLE II. Systematic errors in signal extraction.

| | $\nu_\mu$ channel | $\bar{\nu}_\mu$ channel |
|---|---|---|
| Signal | 159.5±17.3(stat) | 96.7±13.2(stat) |
| $f_{ep/en}$ | 2.2% | 4.5% |
| Slope | 0.6% | 0.8% |
| $Q^2(e^-p,e^+n)$ | 0.3% | 1.2% |
| $e^-p,e^+p$ model | 0.2% | 1.1% |
| Totals | 2.3% | 4.9% |
| Result | 159.5±17.3±3.7 | 96.7±13.2±4.7 |

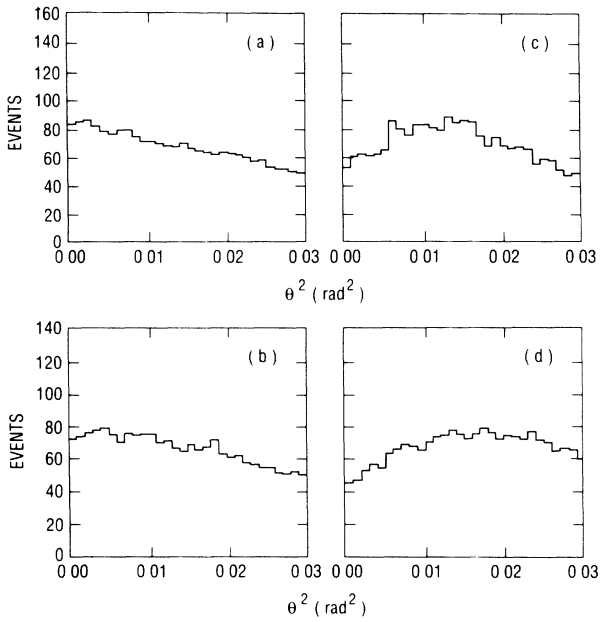


FIG. 11. The individual background distributions after taking account of all smearing effects. (a) $\nu_\mu n \to \bar{\nu}_\mu n\pi^0$, (b) $\bar{\nu}_\mu n \to \bar{\nu}_\mu n\pi^0$, (c) $\nu_e n \to e^- p$, and (d) $\bar{\nu}_e p \to e^+ n$.

where $n_{ij}$ is the number of events in element $ij$ for the data and $\bar{n}_{ij}$ is the expected number of events in the element:

$$\bar{n}_{ij} = N_s S_{ij} + N_b[(1 - f_{(ep/en)})G_i + f_{(ep/en)}Q_i]E_j \ , \tag{12}$$

where $N_s$ is the number of signal events and $N_b$ is the number of background events. $S_{ij}, G_i, Q_i, E_j$ are normalized distributions modeling the signal, photons from pion decay, quasielastics, and the energy distribution of the background, respectively. The indices, $i$ and $j$, run over bins in the two variables, $\theta^2$ and energy.

### E. Signal extraction results

Using the maximum-likelihood method,[21] the number of signal events $N_s$ and the number of background events $N_b$ were allowed to vary to give the best fit (Figs. 12 and 13) for quasielastic fractions of $f_{ep}=0.09$ and $f_{en}=0.55$ over the whole angular region, $\theta^2 < 0.03$ rad$^2$. The number of signal events were

$$N_s(\nu_\mu e \to \nu_\mu e) = 159.5 \pm 17.3(\text{stat}) \pm 3.7(\text{syst})$$

and

$$N_s(\bar{\nu}_\mu e \to \bar{\nu}_\mu e) = 96.7 \pm 13.2(\text{stat}) \pm 4.7(\text{syst}) \ .$$

The systematic error for signal extraction (Table II) was due to four uncertainties: the fraction of the background that was quasielastic, the $Q^2$ region of the quasielastics, the slope effect due to the shower filter, and details of the modeling of the quasielastics which included the choice for $M_A$ and the nuclear scattering. A number of different fits were made by changing the modeling of the background; parameters that affected the shape of the distri-

butions were varied within their errors. For both channels approximately 93% of the signal is in the signal region, $\theta^2 < 0.01$ rad$^2$; the signal to background ratio in this region is

$$S_\nu/N_\nu(\theta^2 < 0.01 \text{ rad}^2) = 0.54 ,$$

$$S_{\bar\nu}/N_{\bar\nu}(\theta^2 < 0.01 \text{ rad}^2) = 0.58$$

and 7.5% (47.0% for $\bar\nu$ data) of the background events in the signal region are due to the electron neutrinos and the rest are due to neutral pions.

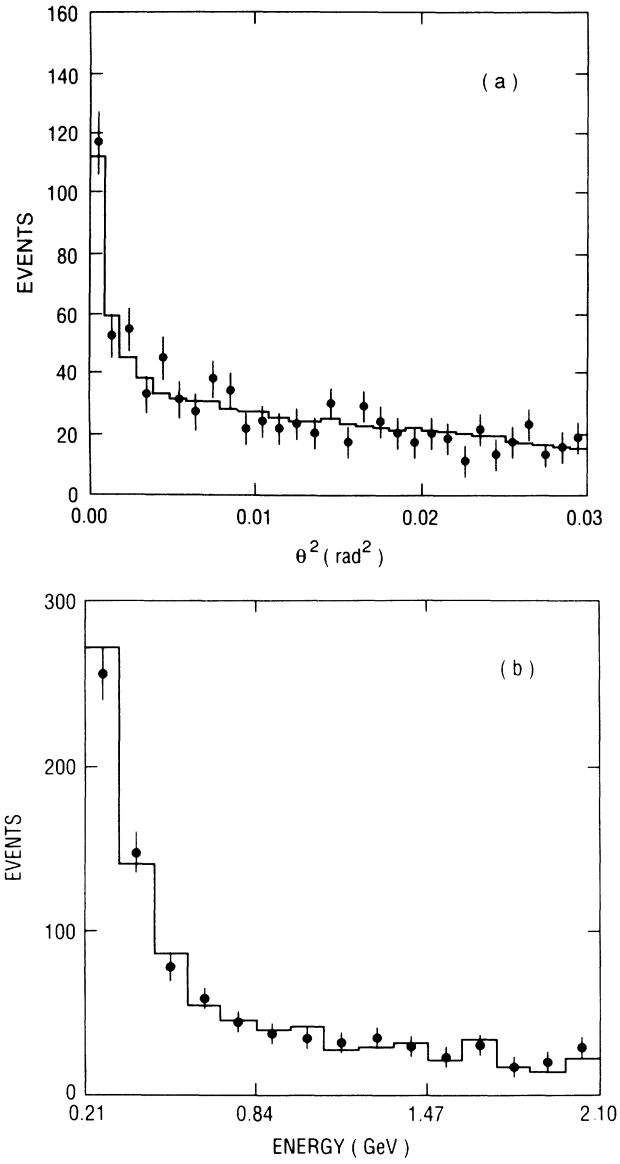


FIG. 12. Distributions for $\nu_\mu$: (a) $\theta^2$ and (b) electron energy. The points are the data and the histograms are the resulting fits to signal plus background.

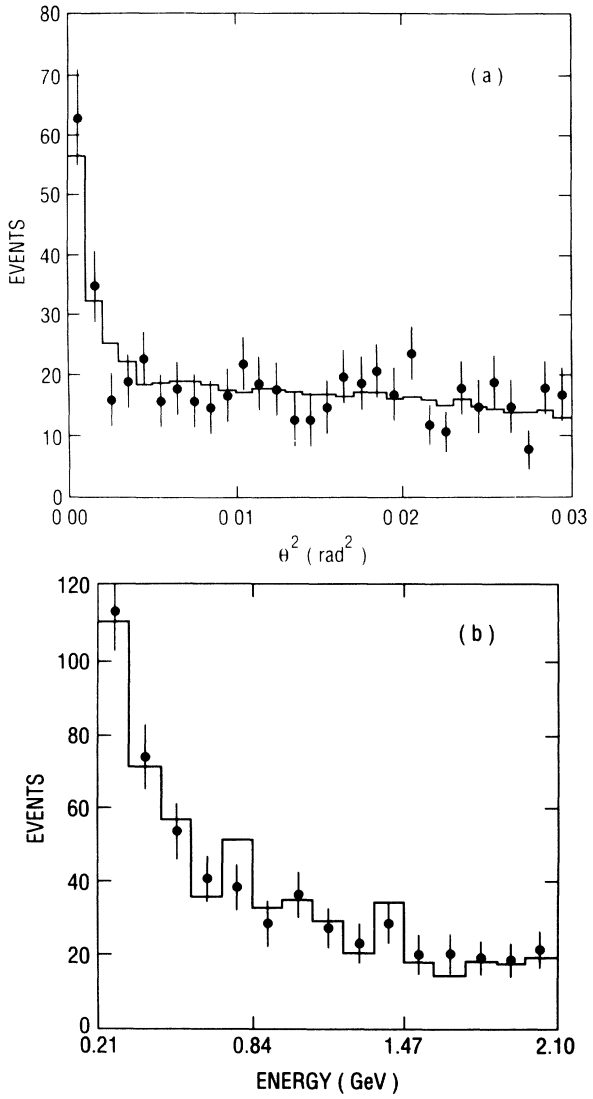


FIG. 13. Distributions for $\bar\nu_\mu$: (a) $\theta^2$ and (b) electron energy. The points are the data and the histograms are the resulting fits to signal plus background.

## IV. ACCEPTANCES AND EFFICIENCIES

The number of signal events had to be corrected for losses due to the various cuts in the analysis and for contaminations. The corrections were studied mainly by Monte Carlo techniques. The statistical error on the determinations are from the finite number of Monte Carlo events used. The various losses in the analysis are considered in their order of significance.

(1) *Energy acceptance* ( $A_{210\to 2100}$ ): The loss due to this cut was evaluated by generating a large number of Monte Carlo events, smearing them by the detector resolution, and applying the energy cut. The acceptance factor depended weakly on the value of the Weinberg angle. Therefore when the value of $\sin^2\theta_W$ was finally evaluated the $\sin^2\theta_W$ dependence of the acceptance was used.

(2) *Software filters and shower filter angle cut*: Detector inefficiencies and noise due to unrelated events caused the software filter to reject some genuine electron events. The efficiency of the software in finding electron shower events was calculated by passing Monte Carlo–generated electron events through the filtering. These were events generated with the full Monte Carlo simulation which contained models for the PDT and calorimeter inefficiencies. In addition, randomly selected data events from different running periods were overlaid on the Monte Carlo events. The efficiency for the software filter was the fraction of events selected from events that were within the energy cut and the fiducial volume. The calculation was done for various combinations of two sets of overlay events and detector element inefficiencies to understand the systematic error. Since the software procedures were upgraded for analysis of the later data, the software efficiencies for the earlier and later data analysis were computed separately, weighted according to the normalization which is discussed in the next section, and combined; the errors were propagated.

(3) *Visual scan efficiency*: The visual scanning efficiency was determined by passing full Monte Carlo events through the same analysis procedure as if they were real events, randomly inserting them among real events in the data, and scanning the entire sample twice during the regular processing. The scanning efficiency ($\epsilon_{\rm vis}$) was determined as the fraction of the Monte Carlo events found by the scanners.

(4) *The vertex energy cut*: This was a small correction which was computed using the full Monte Carlo simulation of electron events.

(5) *The $e/\gamma$ cut*: The loss of events due to this cut was determined by using test beam electron events at various energies. The efficiency, $0.91\pm0.01\pm0.02$, did not depend on the initial energy of the electron.

(6) *The road cut*: The road cut was investigated by passing the full Monte Carlo events through the interactive road cut and determining the fraction accepted by the operator. Some events failed because of unrelated tracks from the overlay events or detector inefficiencies.

(7) *$\theta^2 < 0.03$ rad$^2$ cut*: The small correction due to this angle cut was also investigated by Monte Carlo simulation. Most elastically scattered events were well below 0.03 rad$^2$, but a few events were rejected because of the angular resolution.

(8) *The opposite-helicity contamination*: A fraction of the elastic-scattering events were due to the opposite-helicity neutrinos in the beam. The opposite-helicity flux was measured by the magnetic spectrometer. The number of elastic-scattering events due to the opposite-helicity beam was obtained by calculating the flux-averaged cross section. Since the elastic scattering cross sections have a linear dependence on energy, the flux-averaged cross sections were simply a constant times the mean energy of the beam. Thus the following formula was obtained for the contamination: For the neutrino data,

$$f_{\rm WH}=\frac{f_{\bar{\nu}\nu}}{f_{\bar{\nu}\nu}+(1-f_{\bar{\nu}\nu})\langle E_\nu\rangle R/\langle E_{\bar{\nu}\nu}\rangle} \tag{13a}$$

and for the antineutrino data

$$f_{\rm WH}=\frac{f_{\nu\bar{\nu}}}{f_{\nu\bar{\nu}}+(1-f_{\nu\bar{\nu}})\langle E_{\bar{\nu}}\rangle/\langle E_{\nu\bar{\nu}}\rangle R}\ , \tag{13b}$$

where $f_{\rm WH}$ is the fraction of electron events due to the wrong-helicity neutrinos, $f_{\nu\bar{\nu}}$ ($f_{\bar{\nu}\nu}$) is the contamination of $\nu$ ($\bar{\nu}$) in the $\bar{\nu}$ ($\nu$) beam, $\langle E_\nu\rangle$ is the mean energy of the primary beam, and $\langle E_{\bar{\nu}\nu}\rangle$ is the mean energy of the contamination. The opposite-helicity contamination depends on the elastic-scattering cross sections, in particular on $R$, the ratio of the cross sections, $\sigma_\nu/\sigma_{\bar{\nu}}$. Since we are trying to measure the cross sections and the ratio, this dependence should be carried to the end of the analysis; nevertheless, the corrections due to the opposite-helicity beam were not large, and so the value of $R$ (1.2) computed at the world-average[22] value of $\sin^2\theta_W$ ($0.229\pm0.006$) was used. Since the contamination was different in the last running period, it was computed separately, weighted by the normalization, and combined for the entire data set.

(9) *The wrong-flavor contamination*: A fraction of the electron events were due to the wrong-flavor neutrinos in the beam (i.e., $\nu_e$ in the $\nu_\mu$ beam and $\bar{\nu}_e$ in the $\bar{\nu}_\mu$ beam). The background is due to $\nu_e e\rightarrow\nu_e e$ and $\bar{\nu}_e e\rightarrow\bar{\nu}_e$ reactions. These reactions can occur with both charged- and neutral-current contributions in the standard model; therefore their cross sections are larger than $\nu_\mu e\rightarrow\nu_\mu e$ and $\bar{\nu}_\mu e\rightarrow\bar{\nu}_\mu e$ cross sections. The fraction ($f_{\rm WF}$) of electron events due to $\nu_e e$ or $\bar{\nu}_e e$ was estimated by assuming GWS standard-model cross sections with $\sin^2\theta_W=0.225$ and by assuming the energy of the electron neutrinos to be about the same as the muon neutrinos. The flux of electron neutrinos was estimated from data. The systematic error was mainly from uncertainties in the flux.

TABLE III. Contributions to the overall signal acceptance.

| | |
|---|---|
| $A_{210\rightarrow2100}$ | $0.710\pm0.001\pm0.030$ |
| | $0.710\pm0.001\pm0.010$ |
| $\epsilon_{\rm soft}$ | $0.852\pm0.007\pm0.013$ |
| | $0.914\pm0.011\pm0.020$ |
| $\epsilon_{\rm vis}$ | $0.980\pm0.0022$ |
| | $0.950\pm0.0063$ |
| $\epsilon_{E{\rm vtx}<30}$ | $0.978\pm0.002\pm0.007$ |
| | $0.996\pm0.004\pm0.0$ |
| $\epsilon_{e/\gamma}$ | $0.91\pm0.01\pm0.02$ |
| | $0.91\pm0.01\pm0.02$ |
| $\epsilon_{\rm road}$ | $0.924\pm0.010\pm0.011$ |
| | $0.950\pm0.010\pm0.010$ |
| $\epsilon_{\theta^2<0.03}$ | $0.993\pm0.001\pm0.031$ |
| | $0.993\pm0.001\pm0.030$ |
| $(1-f_{\rm WH})$ | $0.979\pm0.0\pm0.003$ |
| | $0.890\pm0.0\pm0.010$ |
| $(1-f_{\rm WF})$ | $0.964\pm0.0\pm0.009$ |
| | $0.979\pm0.0\pm0.010$ |
| Total corr | $\nu_\mu$ $0.477\pm0.009\pm0.031$ |
| | $\bar{\nu}_\mu$ $0.580\pm0.012\pm0.031$ |

TABLE IV. Systematic errors for signal extraction. The last column lists the correlated errors between reactions (1) and (2).

| Systematic error | $\sigma_\nu$ | $\sigma_{\bar{\nu}}$ | $\sigma_{\nu\bar{\nu}}$ |
|---|---|---|---|
| Signal | 2.3% | 4.9% | |
| $A_{210\to2100}$ | 4.2% | 1.4% | 2.4% |
| $\epsilon_{\text{soft}}$ | 1.5% | 2.2% | 1.8% |
| $\epsilon_{\text{vis}}$ | None | None | |
| $\epsilon_{E\text{vtx}<30}$ | 0.7% | 0.0% | |
| $\epsilon_{e/\gamma}$ | 2.2% | 2.2% | 2.2% |
| $\epsilon_{\text{road}}$ | 1.2% | 1.1% | 1.1% |
| $\epsilon_{\theta^2<0.03}$ | 3.1% | 3.0% | 3.0% |
| $(1-f_{\text{WH}})$ | 0.3% | 1.1% | |
| $(1-f_{\text{WF}})$ | 0.9% | 1.0% | |
| Total | 6.6% | 7.0% | 4.9% |

The corrected total numbers of electron events were obtained by dividing the total number of events observed by the total correction which is computed in Table III:

$$\text{corr}=\frac{A_{210-2100}\sum_i \epsilon_i}{(1-f_{\text{WH}})(1-f_{\text{WF}})} . \tag{14}$$

The corrected total number of $\bar{\nu}_\mu e\to\bar{\nu}_\mu e$ events was

$$N(\nu_\mu e\to\nu_\mu e)=311.0\pm34.2(\text{stat})\pm20.4(\text{syst}) .$$

The corrected total number of $\bar{\nu}_\mu e\to\bar{\nu}_\mu e$ events was:

$$N(\bar{\nu}_\mu e\to\bar{\nu}_\mu e)=159.8\pm22.1(\text{stat})\pm11.1(\text{syst}) .$$

Table IV shows the systematic errors arising from the signal extraction and all the factors contributing to the total correction. Since much of the analysis was the same for neutrino and antineutrino data, some of the systematic error was correlated.

## V. FLUX NORMALIZATION

Measurement of the total incident neutrino-antineutrino flux was necessary for the determination of $\nu_\mu e\to\nu_\mu e$ and $\bar{\nu}_\mu e\to\bar{\nu}_\mu e$ cross sections. The flux was indirectly measured by determining the reaction rates of the muon-neutrino quasielastic interactions: $\nu_\mu n\to\mu^- p$ and $\bar{\nu}_\mu p\to\mu^+ n$. These reactions had a simple topology in the detector. They are the dominant cross sections in the energy range of this experiment; in addition, the differential cross sections for these reactions are well understood[23] and are independent of $\sin^2\theta_W$. These considerations led to the choice of quasielastic event rates as the normalization for this experiment.

### A. Sample selection

A topological selection was used to isolate events containing single long muons produced by the quasielastic interactions. The following cuts were applied to obtain a sample of quasielastic events from the same data set that yielded the elastic-scattering events.

(1) Events with a single fitted track longer than 20 modules, corresponding to muon energy greater than 350 MeV, were selected. This requirement eliminated most charged pions since pions above this energy tend to have a high probability of scattering.

(2) The muon track selected in (1) was required to be within 15° of the beam direction. This restricted the average $Q^2$ to be so low that the proton track was too short to be reconstructed.

(3) Next, the scintillator multiplicity and energy distributions away from the event vertex inside a spatial cylinder (tube cut) surrounding the track were considered. The event was rejected if the average number of scintillators per plane was not close to unity and if the average energy per module was not consistent with $dE/dx$ for a muon. The tube cut removed showers or overlapping multitrack events.

(4) The event vertex was restricted to the same fiducial volume as in the electron analysis.

Because the normalization event sample was not limited by statistics, our primary production program sampled only one out of three events for normalization to save computing time.

### B. Backgrounds and corrections

The primary backgrounds to quasielastic scattering were single-pion inelastic charged-current interactions. The topological selection removed background channels producing more than a single fitted charged track. The remaining single-pion and multipion backgrounds were calculated by Monte Carlo simulations and subtracted from the samples (Table V). The fraction of events in the two normalization samples due to opposite-helicity neu-

TABLE V. Single and multipion background fractions in the flux normalization samples.

| $\nu_\mu$ channel | Fraction in data | | $\bar{\nu}_\mu$ channel |
|---|---|---|---|
| $\mu^- p$ (signal) | 0.563 | 0.598 | $\mu^+ n$(signal) |
| $\mu^- p\pi^+$ | 0.244 | 0.133 | $\mu^+ n\pi^-$ |
| $\mu^- p\pi^0$ | 0.068 | 0.063 | $\mu^+ n\pi^0$ |
| $\mu^- n\pi^+$ | 0.077 | 0.062 | $\mu^+ p\pi^-$ |
| Multipion | 0.024 | 0.020 | Multipion |
| $\mu^+ n$ (wrong helicity) | 0.024 | 0.124 | $\mu^- p$ (wrong helicity) |

TABLE VI. Flux-normalization acceptances and efficiencies.

| Correction | $\nu_\mu$ channel | $\bar{\nu}_\mu$ channel |
|---|---|---|
| Sampling fraction | $\frac{1}{3}$ | $\frac{1}{3}$ |
| Geometric acceptance | 0.172 | 0.317 |
| Tracking efficiency | 0.85 ±0.02 | 0.86 ±0.05 |
| Angle cut efficiency | 0.98 ±0.02 | 0.98 ±0.03 |
| Tube cut efficiency | 0.974±0.010 | 0.986±0.010 |
| Runs processed | 0.954 | 0.965 |
| Total correction | 0.133/3 | 0.254/3 |

trinos was calculated from the measured contaminations in the primary beams.

The acceptances and efficiencies for the quasielastic samples are summarized in Table VI. They were determined by visual scan or by Monte Carlo calculations, and were averaged over the incident neutrino flux. The tracking efficiency was determined by visual scans of raw events entering the track-finding procedure in the production program. The tracking efficiency represents the ability of the event reconstruction program to find muon tracks in the angular range of interest. The inefficiency was due to PDT inefficiency, multiple scattering, and noise from crossing tracks. The tube-cut efficiency was dominated by noise effects. It was measured by overlapping random data on Monte Carlo quasielastic events. The last factor in Table VI corrects for the data tapes that could not be analyzed for normalization events due to computer processing errors but were analyzed for the electromagnetic showers.

TABLE VII. Flux-normalization systematic errors. The third column lists correlations between reactions (1) and (2).

| | $\sigma_\nu$ | $\sigma_{\bar{\nu}}$ | $\sigma_{\nu\bar{\nu}}$ |
|---|---|---|---|
| QE efficiency | | | |
| Track finding | 2% | 2% | 1% |
| Tube cut | 1% | 1% | 0% |
| Angle cut | 2% | 2% | 1% |
| Totals | 2.9% | 3.0% | 1.4% |
| Misc factors | | | |
| Monte Carlo: | | | |
| Nuclear scattering | 1% | 1% | 1% |
| $\pi$ cross sections | 10% | 6% | 7.5% |
| Multi-$\pi$ cross sections | 4% | 3% | 0% |
| $\pi$ scattering | 2% | 2% | 2% |
| Isospin mix | 1% | 1% | 1% |
| $M_A$ | 1% | 1% | 0.5% |
| Pauli exclusion | 2% | 2% | 2% |
| Fermi momentum | 0% | 1% | 0% |
| Beam spectra | 4% | 2% | 0% |
| Wrong helicity | 0% | 2% | 0% |
| Totals | 12.0% | 8.1% | 8.2% |
| Final totals | 12.3% | 8.6% | 8.3% |

### C. Normalization results

The angular distribution of muons from the quasielastic data and the Monte Carlo simulation (including background) agreed well. The normalization samples were not limited by statistics. Some of the systematic errors were correlated between the neutrino and antineutrino normalizations. The systematic errors are shown in Table VII.

The number of quasielastic events corrected for inefficiencies and backgrounds, the mean neutrino energy, and the flux-averaged cross section were determined separately for each running period. The individual flux-averaged neutrino (antineutrino) cross sections before combination were for runs A, B, and C: $0.921\times10^{-38}$ cm$^2$ ($0.396\times10^{-38}$ cm$^2$) and $0.918\times10^{-38}$ cm$^2$ ($0.376\times10^{-38}$ cm$^2$), respectively. When combined together with the mean energies and the cross sections appropriately weighted by the number of quasielastic events, the normalization for the entire data set is then given by the numbers in Table VIII.

## VI. RESULTS

The data from this experiment can be used in several different ways to extract the fundamental quantities: $g_V, g_A, \rho, \sin^2\theta_W$, $f$ (the magnetic moment of the muon neutrino), and $\langle r^2\rangle$ (the mean-square charge radius of the muon neutrino). In the following sections these results are presented.

### A. Using the total elastic cross section

From the corrected number of electron events the cross sections for reactions (1) and (2) were calculated using the

TABLE VIII. Flux-averaged energy, quasielastic cross section, and the total number of quasielastic flux-normalization sample.

| | $\nu_\mu$ channel | $\bar{\nu}_\mu$ channel |
|---|---|---|
| $\langle E_\nu\rangle$ | 1.27 GeV | 1.23 GeV |
| $\langle\sigma_\nu(\mathrm{QE})\rangle$ | $0.919\times10^{-38}$ cm$^2$ | $0.384\times10^{-38}$ cm$^2$ |
| $N_{\mathrm{QE}}$ | $10.1\times10^5$ | $4.26\times10^5$ |

quasielastic normalization. Since the total cross sections depend linearly on the neutrino energy for reactions (1) and (2), the dependence on neutrino energy can be eliminated and a cross section per unit energy defined:

$$\sigma_0 = \frac{\sigma(E_\nu)}{E_\nu} . \tag{15}$$

In terms of the observed quantities, the cross section per unit energy is expressed as

$$\sigma_0 = \frac{N_e}{N_{\rm QE}} \frac{n_{n/p}}{n_e} \frac{\langle \sigma_{\rm QE} \rangle}{\langle E_\nu \rangle} , \tag{16}$$

where $N_e$ is the corrected number of $\nu_\mu e \to \nu_\mu e$ or $\bar{\nu}_\mu e \to \bar{\nu}_\mu e$ events observed in the detector, $n_e$ is the number of target electrons in the fiducial volume of the detector, $N_{\rm QE}$ is the number of quasielastic events observed in the detector, $n_{n/p}$ is the number target nucleons (neutrons for the neutrino quasielastics and protons for the antineutrino quasielastics) in the fiducial volume, $\langle \sigma_{\rm QE} \rangle$ is the flux-averaged cross section for the quasielastic events, and $\langle E_\nu \rangle$ is the mean beam energy. A study of the detector chemistry gave the neutron-to-electron ratio: $n_n/n_e = 0.811$. All the quantities in the expression for the cross section are known: combining them and their errors give the values

$$\frac{\sigma_{\nu_\mu e \to \nu_\mu e}}{\langle E_\nu \rangle} = [1.80 \pm 0.20(\text{stat}) \pm 0.25(\text{syst})] \times 10^{-42} \text{ cm}^2/\text{GeV} ,$$

$$\frac{\sigma_{\bar{\nu}_\mu e \to \bar{\nu}_\mu e}}{\langle E_\nu \rangle} = [1.17 \pm 0.16(\text{stat}) \pm 0.13(\text{syst})] \times 10^{-42} \text{ cm}^2/\text{GeV} .$$

The acceptance factor[17] $A_{210 \to 2100}$ for the electron events was weakly dependent on the particular value of $g_V$ and $g_A$. The dependence was determined from the neutrino spectrum and the differential cross section:

$$A^{\nu}_{\rm corr}(g_V, g_A) = \frac{1.0272(g_V + g_A)^2 + 0.2796(g_V - g_A)^2}{(g_V + g_A)^2 + 1/3(g_V - g_A)^2} , \tag{17a}$$

$$A^{\bar{\nu}}_{\rm corr}(g_V, g_A) = \frac{1.0953(g_V + g_A)^2 + 0.2850(g_V - g_A)^2}{(g_V + g_A)^2 + 1/3(g_V - g_A)^2} . \tag{17b}$$

To determine $g_V$, $g_A$, and $\sin^2\theta_W$ properly, the functional dependence of $A_{210 \to 2100}$ was included in the least-$\chi^2$ fits which extracted $\sin^2\theta_W$ and the relational form of $g_V$ and $g_A$. By using the acceptance correction factors (17a) and (17b) and the measured cross sections, the confidence interval of $g_V$ and $g_A$ was determined from a least-$\chi^2$ fit. The $\chi^2$ function is expressed as

$$\chi^2 = \frac{[\sigma^{\rm th}(g_V, g_A) - \sigma^{\rm expt}/A_{\rm corr}(g_V, g_A)]^2}{[\delta\sigma^{\rm expt}/A_{\rm corr}(g_V, g_A)]^2} , \tag{18}$$

where $\sigma^{\rm th}(g_V, g_A)$ is the theoretical prediction, $\sigma^{\rm expt}$ is the experimental determination of the cross section, $\delta\sigma^{\rm expt}$ is the error on the experimental determination of the cross section, and $A_{\rm corr}(g_V, g_A)$ is the acceptance correction factor. The $\Delta\chi^2 = 1$ confidence-level interval is the region between each pair of ellipses in Fig. 14. With the predictions for $g_V$ and $g_A$ from the GWS model incorporated in the $\chi^2$ function, the electroweak mixing parameter, $\sin^2\theta_W$, was determined: from the $\nu_\mu e \to \nu_\mu e$ cross section alone,

$$\sin^2\theta_W = 0.195^{+0.026}_{-0.020}(\text{stat})^{+0.033}_{-0.025}(\text{syst})$$

and, from the $\bar{\nu}_\mu e \to \bar{\nu}_\mu e$ cross section alone,

$$\sin^2\theta_W = 0.200^{+0.032}_{-0.203}(\text{stat})^{+0.027}_{-0.203}(\text{syst}) ,$$

where the statistical and systematic errors were treated separately. A determination of $\rho$ and $\sin^2\theta_W$ is obtained in a simultaneous two-parameter fit to both cross sections using the correlated systematic errors:

$$\sin^2\theta_W = 0.199^{+0.024}_{-0.025}, \quad \rho = 1.005^{+0.070}_{-0.075} .$$

If $g_V$ and $g_A$ are allowed to vary in a two-parameter fit, confidence intervals are obtained with a fourfold ambiguity (Fig. 14). Only one of the four solutions remains when results of other experiments are taken into account. Only solutions D and C are allowed by $\bar{\nu}_e e$ reactor and $\nu_e e$ accelerator studies,[24] and only D and B are allowed by $e^+e^-$ experiments.[25] Thus only solution D is consistent with all experiments:

$$g_V = -0.102^{+0.039}_{-0.040}(\text{stat})^{+0.029}_{-0.028}(\text{syst}) ,$$

$$g_A = -0.503^{+0.024}_{-0.022}(\text{stat})^{+0.029}_{-0.027}(\text{syst}) .$$

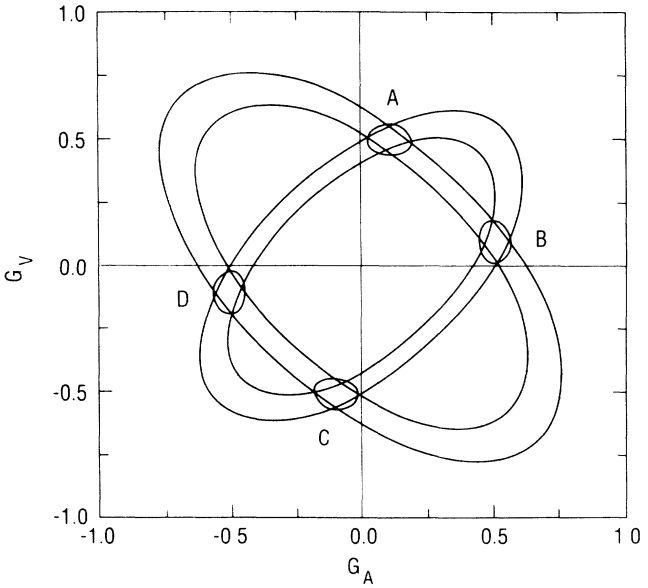


FIG. 14. 68%-confidence-level plot of $g_V$ vs $g_A$ for the cross section for $\nu_\mu e \to \nu_\mu e$ and $\bar{\nu}_\mu e \to \bar{\nu}_\mu e$ scattering and also the combined fit (small regions A, B, C, and D).

The expected relations in the GWS model are given by Eqs. (5) and (6).

### B. Using the cross-section ratio

The results for $\nu_\mu e$ scattering were combined with results for $\bar{\nu}_\mu e$ scattering to get a better determination of $g_V$ and $g_A$ by considering the ratio of two cross sections:

$$R = \frac{\sigma(\nu_\mu e \to \nu_\mu e)}{\sigma(\bar{\nu}_\mu e \to \bar{\nu}_\mu e)} . \tag{19}$$

The ratio is independent of $\rho$; it depends only upon the weak-coupling constants of the electron. Since the determination of each cross section was performed in a similar fashion, many systematic effects cancel, thereby reducing the error in the final determination. The acceptable solutions for $g_V$ and $g_A$ are constrained to within the intersection of the separate solutions for each cross-section determination. Finally, the error on $\sin^2\theta_W$ is less sensitive to the error on the ratio than on the individual cross sections (Fig. 1).

The ratio is determined from a least-$\chi^2$ fit. The $\chi^2$ function is expressed as

$$\chi^2 = \frac{(\sigma_{\nu_\mu e}/A^{\nu}_{\rm corr} - R\sigma_{\bar{\nu}_\mu e}/A^{\bar{\nu}}_{\rm corr})^2}{\delta\sigma^2_{\nu\nu} - 2\delta\sigma^2_{\nu\bar{\nu}}R + \delta\sigma^2_{\bar{\nu}\bar{\nu}}R^2} , \tag{20}$$

where $\sigma_{\nu_\mu e}$ and $\sigma_{\bar{\nu}_\mu e}$ are the measured cross sections for $\nu_\mu e \to \nu_\mu e$ and $\bar{\nu}_\mu e \to \bar{\nu}_\mu e$ scattering, respectively; $\delta\sigma_{\nu\nu}$ and $\delta\sigma_{\bar{\nu}\bar{\nu}}$ are the experimental errors associated with the measured $\nu_\mu e \to \nu_\mu e$ and $\bar{\nu}_\mu e \to \bar{\nu}_\mu e$ cross sections, respectively; $\delta\sigma_{\nu\bar{\nu}}$ is the correlated (systematic) error associated with the two cross-section determinations. The result for the ratio from the $\chi^2$ fit is

$$R = 1.53^{+0.30}_{-0.25}(\text{stat})^{+0.18}_{-0.17}(\text{syst}) ,$$

where the error limits correspond to $\Delta\chi^2 = 1$. From this the electroweak mixing parameter is determined to be

$$\sin^2\theta_W = 0.199^{+0.020}_{-0.019}(\text{stat})^{+0.013}_{-0.013}(\text{syst}) .$$

The $\chi^2$ functions for the separate fits to the cross sections and to the ratio of the cross sections are illustrated in Fig. 15; the minima of all three functions agree well with each other.

### C. Using the differential cross section

The theoretical differential cross section for $\nu_\mu e \to \nu_\mu e$ (upper sign) and $\bar{\nu}_\mu e \to \bar{\nu}_\mu e$ (lower sign) scattering can be approximated at these energies in terms of $g_V$ and $g_A$:

$$\frac{d\sigma}{dy} = \frac{\rho^2 G_F^2 m_e}{2\pi} E_\nu [(g_V \pm g_A)^2 + (g_V \mp g_A)^2(1-y)^2] . \tag{21}$$

The first component in this expression is independent of $y$, while the second component varies as $(1-y)^2$. Because $y = T_e/E_\nu$ and $\theta^2$ are related uniquely through kinematics, the first and second terms in the cross section correspond to two different $\theta^2$ distributions (Fig. 16). Since the cross section is suppressed as $y$ approaches 1 the second

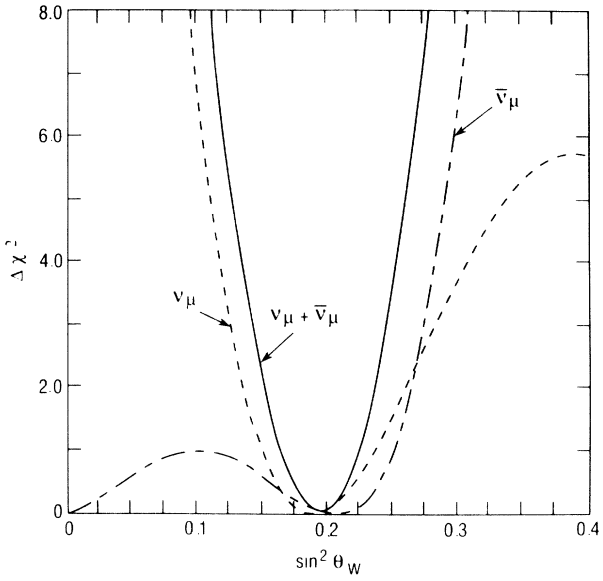


FIG. 15. $\chi^2$ plots for the fits to $\sin^2\theta_W$. Dashed $\nu_\mu$; dash-dot $\bar{\nu}_\mu$; solid $\gamma_\mu$-$\bar{\nu}_\mu$.

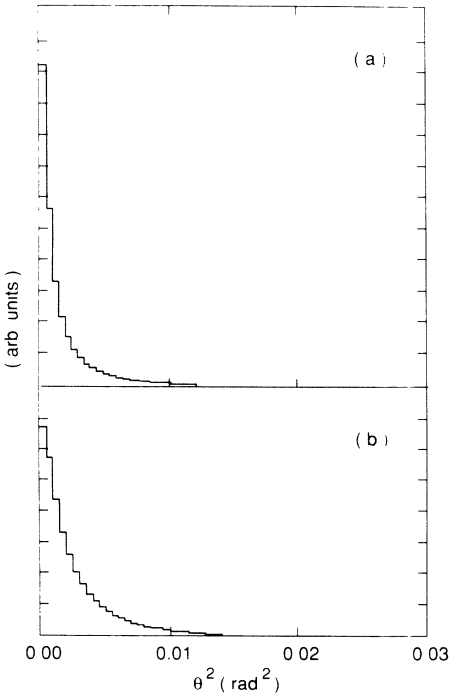


FIG. 16. $\theta^2$ distributions for the two components expected in the differential cross section for $\nu_\mu e \to \nu_\mu e$ scattering; distributions for $\bar{\nu}_\mu e \to \bar{\nu}_\mu e$ scattering are similar. The distributions depend only on the spectrum of neutrinos; the value of $\sin^2\theta_W$ determines the relative contribution of the two distributions in the true distribution. (a) $\theta^2$ distribution for the $y$-independent term. (b) $\theta^2$ distribution for the $(1-y)^2$ term.

term is less sharply peaked in the forward direction. The values of $g_V$ and $g_A$ determine the relative contributions of the two components to the final distributions.

The relatively poor shower energy resolution, compared to the angular resolution, and the uncertainty in neutrino energy due to the wideband spectrum precluded determination of $y$ for each event. Nevertheless, the excellent $\theta^2$ resolution allows fits to be made to more finely binned $\theta^2$ distributions. The $\theta^2$ distributions were binned so that each bin had the width of one standard deviation in the signal region. A likelihood fit was made to the $\theta^2$ distributions using the following function as the parent distribution:

$$n_i = \frac{\rho^2 G_F^2 m_e}{2\pi} F_{\text{norm}} \left[ (g_V \pm g_A)^2 A_1 f_i + (g_V \mp g_A)^2 A_2 \frac{y_i}{3} \right] + N_b b_i \ , \quad (22)$$

$$F_{\text{norm}} = \frac{N_{QE} \langle E_\nu \rangle}{\langle \sigma(QE) \rangle} \ , \quad (23)$$

where the index $i$ runs over the $\theta^2$ bins, $F_{\text{norm}}$ is the quasielastic normalization; $f_i$, $y_i$, and $b_i$ are the normalized $\theta^2$ distributions corresponding to the first term, second term, and the background in the distribution, respectively; $A_1$ and $A_2$ are the acceptances for the first and second terms; $N_b$ is the total number of background events. The upper sign in the formula is for $\nu_\mu e \to \nu_\mu e$ and the lower sign is for $\bar{\nu}_\mu e \to \bar{\nu}_\mu e$ data.

A negative log-likelihood function was calculated by again assuming Poisson statistics in each bin and the package MINUIT was used to minimize the negative log-likelihood function by varying $g_V$, $g_A$, and $N_b$. The function was computed and minimized separately for the neutrino and the antineutrino data. A simultaneous fit was also performed by adding the two functions and minimizing the result. 68% likelihood intervals were obtained for the parameters, $g_V$, $g_A$, $N_b$, and $\sin^2\theta_W$. A consistency check was performed by fitting to the variables $(g_V+g_A)^2$ and $(g_V-g_A)^2$ and confirming that the result obtained was positive.

The best fits to the $\theta^2$ distributions are illustrated in Figs. 17 and 18. The likelihood intervals for the separate fits to the neutrino and the antineutrino data and also the combined fit are illustrated in Fig. 19. Resolving the fourfold ambiguity in the same manner as before (Sec. VI) and with $\rho=1$, results for the couplings and $\sin^2\theta_W$ from the combined fit to both differential cross sections are

$$g_V = -0.107^{+0.035}_{-0.036}(\text{stat})^{+0.029}_{-0.028}(\text{syst}) \ ,$$

$$g_A = -0.514^{+0.023}_{-0.023}(\text{stat})^{+0.029}_{-0.027}(\text{syst}) \ .$$

Assuming parabolic symmetric errors the correlation in the statistical errors is $C_{\text{stat}} = -0.163$, and the correlation in the systematic errors is $C_{\text{syst}} = 0.413$:

$$\sin^2\theta_W = 0.195^{+0.018}_{-0.018}(\text{stat})^{+0.013}_{-0.013}(\text{syst}) \ .$$

There is good agreement between this determination and the one obtained from the total cross sections. Furthermore, the total number of events obtained from the above fits ($168\pm18$ $\nu_\mu e \to \nu_\mu e$ and $99\pm15$ $\bar{\nu}_\mu e \to \bar{\nu}_\mu e$ events) agrees within the errors with the previous determination. These are the best determinations of the coupling constants from this experiment and represent approximately a factor 2 improvement over other determinations. This

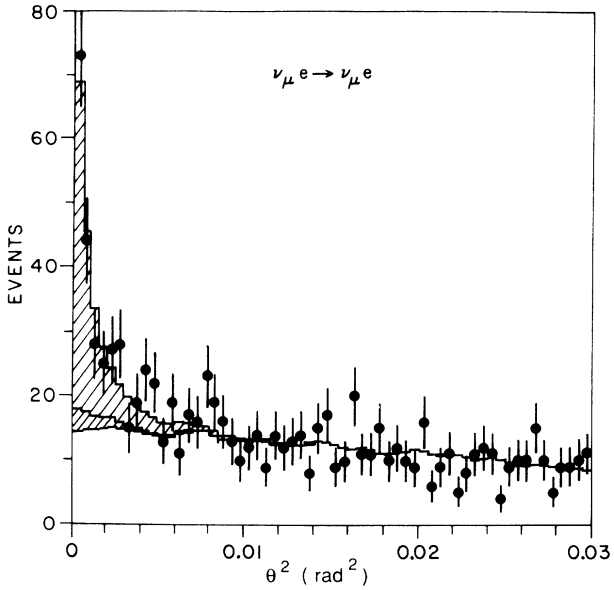


FIG. 17. Differential distributions in $\theta_e^2$ for the neutrino data. Data are points with error bars; $y$-independent term is light shaded; $(1-y)^2$ term is dark shaded and background is unshaded.

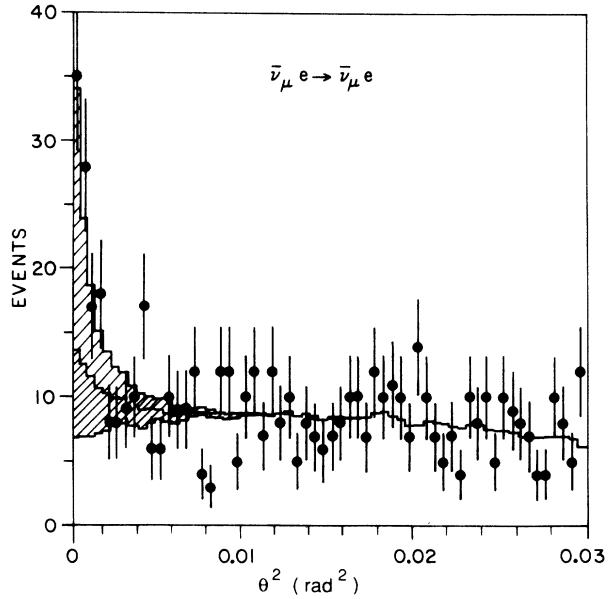


FIG. 18. Differential distributions in $\theta_e^2$ for the antineutrino data. Data are points with error bars; $y$-independent term is light shaded; $(1-y)^2$ term is dark shaded and background is unshaded.

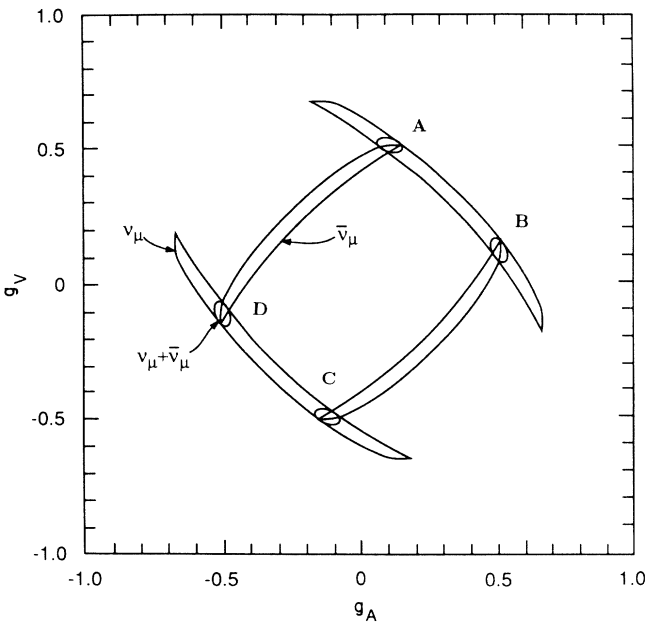


FIG. 19. Likelihood contours for the fits to the neutrino and antineutrino data and also the combined fit. The region outside the contours is excluded. The small regions labeled A–D are for the simultaneous fit to reactions (1) and (2). The projections of the contours give 68% likelihood intervals for $g_V$ and $g_A$ (statistical only).

is the first use of the differential cross sections for this purpose.[16]

### D. Electromagnetic effects

Many gauge theories propose possible electromagnetic properties for the neutrino. The properties may manifest themselves in the form of a magnetic moment or a charge radius.[26,27] They can be tested for as modifications to the theoretical predictions of the cross sections for neutrino interactions.

In this experiment deviations of the cross sections for $\nu_\mu e \to \nu_\mu e$ and $\bar{\nu}_\mu e \to \bar{\nu}_\mu e$ scattering from the predictions of the GWS model for a Weinberg angle determined from non-neutrino experiments can be considered as limits on the existence of electromagnetic effects for the muon neutrino. The limits discussed below were established by performing least-squares fits of the electromagnetic predictions to the experimental determination of the cross sections where the free parameters were the magnitudes of the proposed magnetic moment $f$ and charge radius $\langle r^2 \rangle$ for the muon neutrino. The best results are obtained by performing a fit to both cross sections and utilizing the correlated systematic errors.

The neutrino magnetic moment manifests itself as an additive modification to the total cross section for $\nu_\mu e \to \nu_\mu e$ and $\bar{\nu}_\mu e \to \bar{\nu}_\mu e$ scattering:

$$\sigma^{\rm th} = \sigma^{\rm SM}(\sin^2\theta_W) + \frac{\pi\alpha^2}{m_e^2} f^2 [\ln(E_\nu / E_e^{\rm min}) - 1 + E_e^{\rm min}/E_\nu] , \quad (24)$$

where $\sigma^{\rm SM}(\sin^2\theta_W)$ is the standard-model cross-section prediction without electromagnetic modifications, $f$ is the strength of the magnetic moment for the muon neutrino in units of Bohr magnetons, and $E_e^{\rm min} = 0.2$ GeV is the experimental low-energy cutoff on the recoil electron energy. For purposes of this test, the GWS cross section, $\sigma^{\rm GWS}(\sin^2\theta_W)$ was evaluated at

$$\sin^2\theta_W = 0.230 \pm 0.004({\rm stat}) \pm 0.008({\rm syst}) .$$

This particular value[22] of $\sin^2\theta_W$ represents the best non-neutrino determination, and therefore it is not biased by possible neutrino electromagnetic effects. The 90%-confidence-level limit for the magnetic moment of the muon neutrino is

$$f < 0.85 \times 10^{-9} \text{ Bohr magnetons} .$$

Neutrinos may interact with photons in higher-order processes and thus acquire a charge radius. Thus a deviation in the expected cross section for $\nu_\mu e \to \nu_\mu e$ and $\bar{\nu}_\mu e \to \bar{\nu}_\mu e$ can alternatively be interpreted as a modification to the electroweak mixing parameter, $\sin^2\theta_W$, caused by interference terms due to replacement of the $Z^0$ by a photon. The predictions[16,26] for the cross sections can be expressed as

$$\sigma^{\rm th} = \sigma^{\rm WS}(\sin^2\theta_W + \delta) , \quad (25)$$

$$\delta = \frac{\sqrt{2}\pi\alpha}{3G_F} \langle r^2 \rangle = 3.37 \times 10^{30} \text{ cm}^{-2} \langle r^2 \rangle . \quad (26)$$

Again the best non-neutrino value of $\sin^2\theta_W$ was used. 90%-confidence limits were obtained for the charge radius. If the charge radius is allowed to be negative, a limit can also be obtained for the negative value:

$$(\langle r^2 \rangle) < 0.24 \times 10^{-32} \text{ cm}^2 ,$$
$$(\langle r^2 \rangle) > -2.11 \times 10^{-32} \text{ cm}^2 .$$

## VII. SUMMARY AND CONCLUSIONS

In an experiment at the BNL AGS, the weak-neutral-current coupling constants of the electron were determined from neutrino electron and antineutrino electron elastic scattering. Both the total and, for the first time, differential cross-section measurements were performed. In addition, limits were obtained on the electromagnetic properties of the muon neutrino. Table IX gives a summary of all results from this experiment.

The elastic scattering events were observed in a large mass, finely segmented detector placed in the BNL AGS wideband neutrino beam. A total of $159.5 \pm 17.3 \pm 3.7$ $\nu_\mu e \to \nu_\mu e$ reactions and $96.7 \pm 13.2 \pm 4.7$ $\bar{\nu}_\mu e \to \bar{\nu}_\mu e$ reactions were observed. These observations together with quasielastic normalization yielded the cross sections

$$\sigma(\nu_\mu e \to \nu_\mu e) = [1.80 \pm 0.20({\rm stat}) \pm 0.25({\rm syst})] \times 10^{-42} \text{ cm}^2/\text{GeV} ,$$
$$\sigma(\bar{\nu}_\mu e \to \bar{\nu}_\mu e) = [1.17 \pm 0.16({\rm stat}) \pm 0.13({\rm syst})] \times 10^{-42} \text{ cm}^2/\text{GeV} .$$

TABLE IX. Summary of results from this experiment.

| Final results of this experiment | |
|---|---|
| $N(\nu_\mu e \to \nu_\mu e)$ | $160\pm17\pm4$ |
| $N(\bar{\nu}_\mu e \to \bar{\nu}_\mu e)$ | $97\pm13\pm5$ |
| **Total-cross-section results** | |
| $\frac{\sigma(\nu_\mu e)}{\langle E_\nu \rangle}$ | $(1.80\pm0.20\pm0.25)\times10^{-42}$ cm$^2$/GeV |
| $\frac{\sigma(\bar{\nu}_\mu e)}{\langle E_{\bar{\nu}} \rangle}$ | $(1.17\pm0.16\pm0.13)\times10^{-42}$ cm$^2$/GeV |
| $R$ | $1.53^{+0.30}_{-0.25}$(stat)$^{+0.18}_{-0.17}$(syst) |
| $\rho$ | $1.005^{+0.070}_{-0.075}$ |
| $\sin^2\theta_W$ | $0.199\pm0.020$(stat)$\pm0.013$(syst) |
| **The $\theta^2$ distribution fits** | |
| $g_V$ | $-0.107\pm0.035$(stat)$\pm0.028$(syst) |
| $g_A$ | $-0.514\pm0.023$(stat)$\pm0.028$(syst) |
| $\sin^2\theta_W$ | $0.195\pm0.018$(stat)$\pm0.013$(syst) |
| **$f, \langle r^2 \rangle$ upper limits** | |
| $f$ | $0.85\times10^{-9}$ Bohr magnetons |
| $\langle r^2 \rangle$ | $0.24\times10^{-32}$ cm$^2$ |

By taking the correlated systematic errors into account, the ratio of the two cross sections was determined to be $1.53^{+0.30+0.18}_{-0.25-0.17}$ while values obtained for the weak neutral-current coupling constants of the electron were determined to be $g_V=-0.102^{+0.039+0.029}_{-0.040-0.028}$; $g_A=-0.503^{+0.024+0.029}_{-0.022-0.027}$. The ratio of the neutral-to-charge-current coupling was determined to be $\rho=1.005^{+0.070}_{-0.075}$. By using the predictions of the GWS model for $g_V, g_A$, the Weinberg angle was determined using the ratio method to be

$$\sin^2\theta_W=0.199^{+0.020}_{-0.019}(\text{stat})^{+0.013}_{-0.013}(\text{syst}) .$$

Simultaneous likelihood fits to the angular distributions of the events yielded a measurement of the differential cross sections which agree well with the GWS model predictions of the structure of the neutral current. The differential distribution fits give a value of the Weinberg angle,

$$\sin^2\theta_W=0.195^{+0.018}_{-0.018}(\text{stat})^{+0.013}_{-0.013}(\text{syst}) ,$$

which was more precise than that obtained from the cross-section ratio. Similarly, the differential distributions provide slightly more precise values of $g_V$ and $g_A$:

$$g_V=-0.107\pm0.035(\text{stat})\pm0.028(\text{syst}) ,$$

$$g_A=-0.514\pm0.023(\text{stat})\pm0.028(\text{syst}) .$$

Limits were placed on the muon neutrino magnetic moment and charge radius by examining deviations of the cross sections from the GWS model values, determined by using the value of $\sin^2\theta_W$ given by the measured masses of the intermediate vector bosons. The magnetic moment was determined to be less than $0.85\times10^{-9}$ Bohr magnetons while the charge radius was determined to be $-2.11\times10^{-32}$ cm$^2$ $<\langle r^2 \rangle<0.24\times10^{-32}$ cm$^2$. These limits improve upon our previous measurements[12,16] and of other direct[26,27] measurements or analyses for these quantities. Model-dependent astrophysical and cosmological arguments do set lower bounds on the magnetic moment.[28]

The recent comprehensive analysis of the weak neutral current and the intermediate boson masses by Amaldi *et al.*[22] has included relevant published data on $\nu-q$, $\nu-e$, $e^+-e^-$, $e-q$, and $\bar{q}-q$ reactions. In the analysis of Ref. 22 radiative effects have been included appropriate to the extraction of $\sin^2\theta_W$. Only data published prior to 1986 are included in the Ref. 22 analysis for $\nu_\mu e$ and $\bar{\nu}_\mu e$ scattering; and as a result only a small portion (45%) of the data from this experiment was included in their analysis. Because the full sample of this experiment ($N_\nu=160$, $N_{\bar{\nu}}=98$) together with the final CHARM-I sample[29] ($N_\nu=83$, $N_{\bar{\nu}}=112$) constitute 84% of the world's published data on reactions (1) and (2) and because for each experiment the two reactions were studied in the same detector with similar systematic errors, it is appropriate to combine results of this experiment with those of the CHARM-I Collaboration.

There are several points of contact between the two experiments to check for consistency between them: the individual neutrino and antineutrino cross sections, the ratio $R$ and the couplings $g_V$ and $g_A$. In all cases, the results are in agreement; therefore (1) combining the results of the total-cross-section ratio analysis from the two experiments gives

$$\sin^2\theta_W=0.203\pm0.020 ,$$

and (2) combining the best value from the differential-cross-section analysis from the present experiment with the CHARM-I ratio result we find

$$\sin^2\theta_W=0.199\pm0.019 ,$$

where it has been assumed the statistical and the systematic errors can be combined quadratically. Note that the above values for $\sin^2\theta_W$ have not been radiatively corrected, but these corrections are very small (+0.002). Thus the two experiments with the largest statistics and the best systematics for $\nu_\mu e$ and $\bar{\nu}_\mu e$ scattering suggest a lower principal value for $\sin^2\theta_W$ than do the high-$Q^2$ experiments although they are still in agreement within two standard deviations.

## ACKNOWLEDGMENTS

This experiment would not have been possible without the important assistance of many people. We wish to acknowledge the encouragement we received from R. R. Rau and N. P. Samios through the Brookhaven High Energy Physics Program, the outstanding technical support

of F. Simes, T. Erickson, E. Hassell, S. Marino, M. Van Lith, W. Walker, and the AGS staff at BNL, the technical staff of each of our institutions, and comments and suggestions from J. E. Kim, P. Langacker, W. Marciano, S. Petcov, R. Shrock, and K. Winter. Funding was provided in part by the participating institutions, the U.S. Department of Energy, and the Japanese Ministry of Education, Science and Culture through the Japan-U.S.A. Cooperative Research Project on High Energy Physics.

---

[a]Deceased.
[b]Now at Singer Co., Kearfott Div., Wayne, NJ 07470.
[c]Now at Department of Physics, Hiroshima University, Hiroshima 730, Japan.
[d]Now at Los Alamos National Laboratory, Los Alamos, NM 87545.
[e]Now at Jet Propulsion Laboratory, California Institute of Technology, Pasadena, CA 91125.
[f]Now at Department of Physics, Stanford University, Stanford, CA 94305.
[g]Now at Grumman Aerospace, Bethpage, Long Island, NY 11793.
[h]Now at National Laboratory for High Energy Physics (KEK), Ibaraki-Ken 305, Japan.
[i]Now at Institute for Cosmic Ray Research, University of Tokyo, Tokyo 118, Japan.
[j]Now at Sumitomo Heavy Industry, Tokyo, Japan.
[k]Now at Toshiba, Kawasaki 210, Japan.
[l]Now at Department of Physics, Christopher Newport College, Newport News, VA 23606.
[m]Now at Department of Physics, Ohio State University, Columbus, OH 43210.
[n]Now at Lockheed Aerospace Corp., Sunnyvale, CA 94304.
[o]Now at Lincoln Laboratory, Massachusetts Institute of Technology, Lexington, MA 02173.
[p]Now at Laboratory for Nuclear Studies, Cornell University, Ithaca, NY 14853.
[q]Now at Department of Physics, Northern Illinois University, Dekalb, IL 60115.
[r]Now at Department of Physics, University of Pittsburgh, Pittsburgh, PA 15260.

[1]L. A. Ahrens *et al.*, Nucl. Instrum. Methods **A254**, 515 (1987).
[2]S. L. Glashow, Nucl. Phys. **22**, 579 (1961).
[3]A. Salam, in *Elementary Particle Theory: Relativistic Groups and Analyticity (Nobel Symposium No. 8)*, edited by N. Svartholm (Almqvist and Wiksell, Stockholm, 1968).
[4]S. Weinberg, Phys. Rev. Lett. **19**, 1264 (1967).
[5]L. A. Ahrens *et al.*, Phys. Rev. D **34**, 75 (1986).
[6]L. A. Ahrens *et al.*, Phys. Rev. D **23**, 2732 (1985). NUBEAM is a neutrino-beam simulator program by C. Visser, CERN Hydra Application Library; modifications for this experiment were made by R. Carlini and a copy of this version of the program can be obtained from one of the present authors (D.H.W.).
[7]B. W. Hughlock, Ph.D. thesis, Brown University, 1983.
[8]S. Tatsumi, Ph.D. thesis, Osaka University, 1984.
[9]D. C. Doughty, Ph.D. thesis, University of Pennsylvania, 1984.
[10]L. A. Ahrens *et al.*, Phys. Rev. D **35**, 785 (1987); E. G. Stern, Ph.D. thesis, State University of New York at Stony Brook, 1986.
[11]M. B. Hurley, Ph.D. thesis, University of Pennsylvania, 1984.
[12]J. L. Callas, Ph.D. thesis, Brown University, 1987.
[13]K. Abe *et al.*, Phys. Rev. Lett. **58**, 636 (1987).
[14]L. A. Ahrens *et al.*, Phys. Rev. Lett. **51**, 1514 (1983).
[15]L. A. Ahrens *et al.*, Phys. Rev. Lett. **54**, 18 (1985).
[16]K. Abe *et al.*, Phys. Rev. Lett. **62**, 1709 (1989); K. Abe *et al.*, *ibid.* **58**, 636 (1987). We note that in this latter reference and in Ref. 12, the factor $\sqrt{2}$ in Eq. (26) was inadvertently placed in the denominator instead of the numerator, thus giving an apparently poorer limit in those papers.
[17]M. V. Diwan, Brown University Report No. C00-3130TC-38, 1988 (unpublished).
[18]R. L. Ford and W. P. Nelson, Stanford University Report No. SLAC-210 EGS, Version IV (unpublished).
[19]D. Rein and L. M. Sehgal, Ann. Phys. (N.Y.) **133**, 79 (1981).
[20]C. H. Llewelyn Smith, Phys. Rep. **3C**, 261 (1972).
[21]F. James and M. Roos, Comput. Phys. Commun. **10**, 343 (1975).
[22]U. Amaldi *et al.*, Phys. Rev. D **36**, 1385 (1987).
[23]N. J. Baker *et al.*, Phys. Rev. D **23**, 2499 (1981).
[24]F. Reines, H. S. Gurr, and H. W. Sobel, Phys. Rev. Lett. **37**, 315 (1976); W. Krenz, Aachen University Report No. PITHA 82/26, 1982 (unpublished); R. C. Allen *et al.*, Phys. Rev. Lett. **55**, 2401 (1985).
[25]CELLO Collaboration, H. J. Behrend *et al.*, Z. Phys. C **16**, 301 (1983); JADE Collaboration, W. Bartel *et al.*, Phys. Lett. **99B**, 281 (1981); Mark J Collaboration, D. P. Barber *et al.*, Phys. Rev. Lett. **46**, 1663 (1981); TASSO Collaboration, R. Brandelik *et al.*, Phys. Lett. **117B**, 365 (1982).
[26]See, for example, J. E. Kim, V. Mathur, and S. Okubo, Phys. Rev. D **9**, 3050 (1974); J. E. Kim, *ibid.* **14**, 3000 (1976); B. W. Lee and R. E. Shrock, *ibid.* **16**, 1444 (1977); W. J. Marciano and A. I. Sanda, Phys. Lett. **67B**, 303 (1977); M. A. Beg *et al.*, Phys. Rev. D **17**, 1395 (1978); M. Mohopatra and R. Marshak, Phys. Lett. **91B**, 222 (1980): D. Grosser, *ibid.* **166B**, 340 (1986); M. J. Duncan *et al.*, University of Pennsylvania and University of Barcelona reports, 1987 (unpublished); R. Shrock, Nucl. Phys. **B206**, 259 (1982); S. T. Petcov, Phys. Lett. **115B**, 401 (1983).
[27]J. E. Kim, V. Mathur, and S. Okubo, Phys. Rev. D **9**, 3050 (1974); A. V. Kyuldiev, Nucl. Phys. **B243**, 387 (1984); T. Kebbeker, Ph.D. thesis, University Hamburg, 1986.
[28]J. Bernstein, M. Ruderman, and G. Feinberg, Phys. Rev. **132**, 1227 (1963); K. Fujikawa and R. E. Shrock, Phys. Rev. Lett. **45**, 963 (1980); J. Morgan, Phys. Lett. **102B**, 247 (1981); M. Fukugita *et al.*, Berkeley Astrophysics report, 1987.
[29]CHARM-I Collaboration, J. Dorenbosch *et al.*, Z. Phys. C **41**, 567 (1989).